

Optimization and Generation in Aerodynamics Inverse Design

Huaguan Chen ^{† 1} Ning Lin ^{† 1} Luxi Chen ^{† 1} Rui Zhang ¹ Wenbing Huang ¹ Chongxuan Li ¹ Hao Sun ^{* 1}

Abstract

Inverse design with physics-based objectives is challenging because it couples high-dimensional geometry with expensive simulations, as exemplified by aerodynamic shape optimization for drag reduction. We revisit inverse design through two canonical solutions, the optimal design point and the optimal design distribution, and relate them to optimization and guided generation. Building on this view, we propose a new training loss for cost predictors and a density-gradient optimization method that improves objectives while preserving plausible shapes. We further unify existing training-free guided generation methods. To address their inability to approximate conditional covariance in high dimensions, we develop a time- and memory-efficient algorithm for approximate covariance estimation. Experiments on a controlled 2D study and high-fidelity 3D aerodynamic benchmarks (car and aircraft), validated by OpenFOAM simulations and miniature wind-tunnel tests with 3D-printed prototypes, demonstrate consistent gains in both optimization and guided generation. Additional offline RL results further support the generality of our approach.

1. Introduction

Inverse design is fundamental yet challenging across physics and engineering (Tarantola, 2005). In aerodynamic design, the shape of an aircraft or a road vehicle strongly influences energy efficiency and overall performance: lift and drag are key metrics for aircraft (Anderson, 1999), and aerodynamic drag is a dominant source of resistance for vehicles at highway speeds (Hucho, 2013). Conventional aerodynamic shape optimization relies on repeated design updates

[†]Equal contribution. ¹Gaoling School of Artificial Intelligence, Renmin University of China, Beijing, China. Emails: Huaguan Chen <huaguanchen@ruc.edu.cn>, Ning Lin <ninglin00@outlook.com>, and Luxi Chen <clx1489@ruc.edu.cn>. Correspondence to: Hao Sun <hao-sun@ruc.edu.cn>.

Preprint. February 6, 2026.

coupled with high-cost computational fluid dynamics simulations, which substantially limits broad exploration of the design space (Smith et al., 2006). In recent years, data-driven deep learning methods have emerged as a promising alternative by accelerating aerodynamic evaluation and enabling more efficient shape refinement.

Most existing deep-learning work in aerodynamics focuses on speeding up traditional solvers or building surrogate models for forward prediction (Bhatnagar et al., 2019; Brunton et al., 2020; Li et al., 2020; Wu et al., 2024). In contrast, a unified framework for addressing the inverse design, where one directly optimizes shape under aerodynamic objectives, remains largely missing.

A turning point came in 2024. Tran et al. (2024) proposed an autoencoder that jointly learns geometry reconstruction and drag prediction, enabling car-shape optimization in latent space. Vatani et al. (2025) improved geometric fidelity with a triplane VAE (Peng et al., 2020; Chan et al., 2022) and optimized shapes by partially fine-tuning the model. Hao et al. (2025) incorporated 3D diffusion models (Ho et al., 2020) to expand beyond the training distribution. You et al. (2025) trained a flow-matching generative model (Lipman et al., 2023) and introduced SDF based mesh generation.

Despite this progress, gaps remain. Existing studies have largely emphasized engineering implementations, while a theoretically clear account of how inverse design connects to optimization and generation remains missing. On the optimization side, prior methods often introduce intricate regularization terms to maintain shape stability, which often requires careful tuning of shape-control or regularization parameters to avoid irregular or oscillatory geometries. On the generation side, the guidance strategy commonly adopted in these works (Chung et al., 2022) suffer from a systematic scale bias in the guidance term (Song et al., 2023; Boys et al., 2024). Even with state-of-the-art guidance schemes, covariance variance estimation remains a bottleneck.

We summarize our **contributions** and organize the theoretical part as follows. Sec. 2.1 formalizes point and distributional solutions and relate them to shape-preserving optimization and guided generation. Building on this relationship, Sec. 2.2 introduces a new training loss for the cost predictor, and Sec. 2.3 proposes a shape-preserving optimization method that improves the design objective while

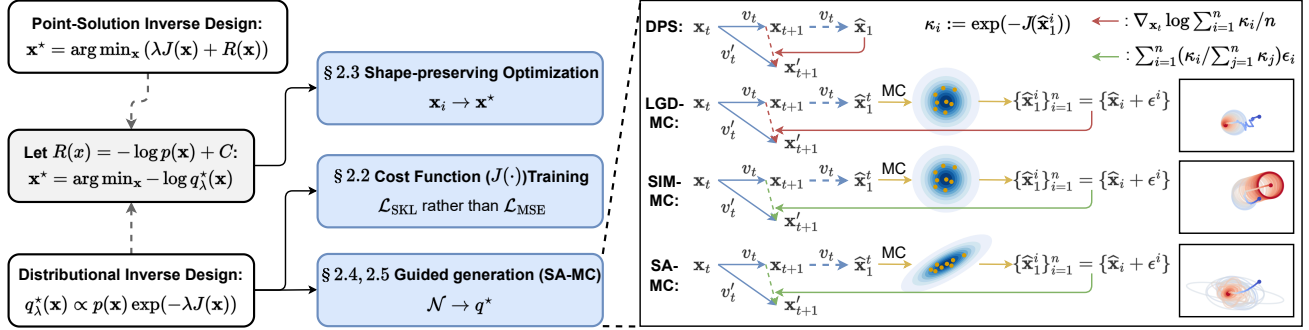


Figure 1. Inverse-design optimality and covariance-aware guidance. The left panel illustrates two classical paradigms in inverse design, point design and distributional design, and highlights their connection. The blue boxes indicate the organization of our theoretical sections. The right panel compares four representative guidance mechanisms, showing their computational graphs and differences. The schematic plots on the far right visualize the distinct trajectory patterns induced by different methods. Circles and ellipses denote variance.

keeping the shape stable. For generation, Sec. 2.4 organizes existing guidance estimators and shows that the gap between two main families is controlled by their covariance approximations, implying that neither recovers the variance-matching Gaussian approximation in general. Sec. 2.5 then presents a new algorithm that approximately estimates this covariance in high-dimensional settings at a modest time and memory cost. The organization is illustrated in Fig. 1.

2. Theory

2.1. Problem Formulation

Let \mathbf{x} denote a design sampled from a data distribution p . We evaluate each design using a cost function $J(\mathbf{x})$. In inverse design, we also introduce a constraint term $R(\mathbf{x})$ and a prior distribution $p_0(\mathbf{x})$. Following Tarantola (2005), we consider a point solution and a distributional solution,

$$\mathbf{x}_\lambda^* := \arg \min_{\mathbf{x}} [\lambda J(\mathbf{x}) + R(\mathbf{x})], \quad (1a)$$

$$q_\lambda^*(\mathbf{x}) \propto p_0(\mathbf{x}) \exp(-\lambda J(\mathbf{x})). \quad (1b)$$

A common choice is $R(\mathbf{x}) = -\log p_0(\mathbf{x}) + C$ with constant C . In this case, q_λ^* is the Gibbs posterior induced by $J(\mathbf{x})$, and the point solution is its MAP estimate:

$$\mathbf{x}_\lambda^* = \arg \min_{\mathbf{x}} -\log q_\lambda^*(\mathbf{x}). \quad (2)$$

We focus on shape-preserving constraints, where designs should remain within the data manifold. We enforce this by setting the prior to the data distribution, $p_0 = p$. Under this choice, the optimal distribution in Eq. 1b is equivalently characterized as the minimizer of

$$\mathcal{J}^{(\lambda)}(q) := \text{KL}(q \parallel p) + \lambda \mathbb{E}_{\mathbf{x} \sim q}[J(\mathbf{x})], \quad (3)$$

which yields the closed form

$$q_\lambda^*(\mathbf{x}) =: p^{(J,\lambda)}(\mathbf{x}) \propto p(\mathbf{x}) \exp(-\lambda J(\mathbf{x})). \quad (4)$$

With $p_0 = p$, Eq. 2 yields a single optimized design (the point solution), whereas Eq. 4 defines a target distribution

for generating multiple designs (the distributional solution). When p is represented by a generative model that maps a simple noise distribution to p , sampling from $p^{(J,\lambda)}$ corresponds to guided generation.

2.2. Cost Function Training

We train a cost predictor J_θ to approximate the true cost J . A natural objective is to minimize the variational objective $\mathcal{J}^{(\lambda)}$ in Eq. 3 evaluated at the distribution $p^{(J_\theta, \lambda)}$:

$$\mathcal{J}^{(\lambda)}(\theta) := \mathcal{J}^{(\lambda)}\left(p^{(J_\theta, \lambda)}\right) = \text{KL}\left(p^{(J_\theta, \lambda)} \parallel p^{(J, \lambda)}\right). \quad (5)$$

This objective is a distributional discrepancy with $p^{(J, \lambda)}$, it naturally extends to a broader class of f -divergences:

$$\mathcal{J}_f^{(\lambda)}(\theta) := D_f\left(p^{(J_\theta, \lambda)}(\mathbf{x}) \parallel p^{(J, \lambda)}(\mathbf{x})\right). \quad (6)$$

In particular, choosing $f(x) = (x - 1) \ln x$ yields the symmetric KL divergence, which admits the compact expression

$$\begin{aligned} \mathcal{J}_{\text{SKL}}^{(\lambda)}(\theta) &= \mathbb{E}_{p(\mathbf{x})}[\lambda(J_\theta(\mathbf{x}) - J(\mathbf{x})) \\ &\quad \cdot (w^{(J, \lambda)}(\mathbf{x}) - w^{(J_\theta, \lambda)}(\mathbf{x})). \end{aligned} \quad (7)$$

$$w^{(J, \lambda)}(\mathbf{x}) = \exp(-\lambda J(\mathbf{x}))/\mathbb{E}_{p(\mathbf{x})}[\exp(-\lambda J(\mathbf{x})].$$

For practical training, we approximate the expectation over p with a minibatch $\mathcal{B} = \{\mathbf{x}_i\}$:

$$\begin{aligned} \mathcal{L}_{\text{SKL}}^{(\lambda)}(\mathcal{B}, \theta) &= \frac{1}{|\mathcal{B}|} \sum_{\mathbf{x} \in \mathcal{B}} \lambda(J_\theta(\mathbf{x}) - J(\mathbf{x})) \\ &\quad \cdot (w_{\mathcal{B}}^{(J, \lambda)}(\mathbf{x}) - w_{\mathcal{B}}^{(J_\theta, \lambda)}(\mathbf{x})), \end{aligned} \quad (8)$$

$$w_{\mathcal{B}}^{(J, \lambda)}(\mathbf{x}) = |\mathcal{B}| \left[\text{softmax}(\{-\lambda J(\mathbf{x}')\}_{\mathbf{x}' \in \mathcal{B}}) \right]_{\mathbf{x}}.$$

A direct implementation would require a separate predictor for each λ , because λ appears explicitly in Eq. 8. To avoid this, we follow the practice in diffusion models of conditioning on the time variable, and treat λ as an additional input to the cost network. Concretely, we replace term of $\lambda J_\theta(\mathbf{x})$ in Eq. 8 with a λ -conditioned prediction $J_\theta(\mathbf{x}, \lambda)$. Relationship between \mathcal{L}_{SKL} and MSE is discussed in App. C.1.

2.3. Shape-preserving Optimization

Following Eq. 2 and Eq. 4, in the optimization setting, we seek the most probable design under the distribution $p^{(J,\lambda)}$:

$$\mathbf{x}^* = \arg \min_{\mathbf{x}} -\log p^{(J,\lambda)}(\mathbf{x}). \quad (9)$$

We use a gradient-based update. The negative log-density gradient separates into an objective term and a score term:

$$-\nabla_{\mathbf{x}} \log p^{(J,\lambda)}(\mathbf{x}) = \nabla_{\mathbf{x}} J(\mathbf{x}, \lambda) - \nabla_{\mathbf{x}} \log p(\mathbf{x}), \quad (10)$$

where $\nabla_{\mathbf{x}} J(\mathbf{x}, \lambda)$ is obtained analytically or by automatic differentiation. The score $\nabla_{\mathbf{x}} \log p(\mathbf{x})$ is estimated using the velocity field of a flow-matching model.

Let $a_t = \dot{\sigma}_t/\sigma_t$, $b_t = (\dot{\alpha}_t\sigma_t - \dot{\sigma}_t\alpha_t)/\sigma_t$ and $s_t = b_t\sigma_t^2/\alpha_t$. Using the connection between the velocity field and the score function (Lipman et al., 2024), we have

$$\begin{aligned} \mathbf{v}_t(\mathbf{x}_t) &= (\dot{\alpha}_t/\alpha_t)\mathbf{x}_t - b_t\sigma_t^2/\alpha_t \cdot \nabla_{\mathbf{x}_t} \log p_t(\mathbf{x}_t), \\ &\Rightarrow -\nabla_{\mathbf{x}} \log p_t(\mathbf{x}) = (\mathbf{v}_t(\mathbf{x}) - (\dot{\alpha}_t/\alpha_t)\mathbf{x})/s_t. \end{aligned} \quad (11)$$

As $t \rightarrow 1$, $s_t \rightarrow 0$ in Eq. 11, which can destabilize the score estimate. We therefore estimate the score at $t < 1$ and apply time annealing (Wang et al., 2023): we sample $t \sim \mathcal{U}(t_{\min}, t_{\max})$ with an increasing t_{\min} over iterations, and inject noise into the iterate. This leads to the approximation

$$\begin{aligned} -\nabla_{\mathbf{x}} \log p^{(J,\lambda)}(\mathbf{x}) &\approx \nabla_{\mathbf{x}} J(\mathbf{x}) - \\ &\mathbb{E}_{t \sim \mathcal{U}(t_{\min}, t_{\max})} [(\mathbf{v}_t(\mathbf{x}_t) - (\dot{\alpha}_t/\alpha_t)\mathbf{x}_t)/s_t]. \end{aligned} \quad (12)$$

In practice, we use $t_{\min} \geq 0.02$ and $t_{\max} \leq 0.98$.

2.4. Guided Generation Background

As discussed in Sec. 2.1, given a flow matching model $\mathcal{N} \rightarrow p$, we add a guidance term \mathbf{g}_t to the velocity field \mathbf{v}_t to steer the transport toward the target distribution $p^{(J,\lambda)}$. Following Eq. 11, \mathbf{g}_t involves the stochastic gradient

$$\mathbf{g}_t = b_t\sigma_t^2/\alpha_t \cdot \nabla_{\mathbf{x}_t} \log \mathbb{E}_{p_{1|t}(\mathbf{x}_1)} [\exp(-J(\mathbf{x}_1, \lambda))] \quad (13)$$

For clarity, we rewrite this term in an equivalent score form and omit λ in the notation. Define the tilted conditional $p_{1|t}^{(J)}(\mathbf{x}_1 | \mathbf{x}_t) \propto p_{1|t}(\mathbf{x}_1 | \mathbf{x}_t) \exp(-J(\mathbf{x}_1))$. Then,

$$\mathbf{g}_t = b_t\sigma_t^2/\alpha_t \cdot \mathbb{E}_{p_{1|t}^{(J)}(\mathbf{x}_1)} [\nabla_{\mathbf{x}_t} \log p_{1|t}(\mathbf{x}_1)]. \quad (14)$$

Estimating Eq. 14 requires sampling from $p_{1|t}(\cdot | \mathbf{x}_t)$ or approximating it. A common approach introduces a proposal $q_{1|t}(\mathbf{x}_1 | \mathbf{x}_t)$ and its tilted version $q_{1|t}^{(J)}(\mathbf{x}_1 | \mathbf{x}_t) \propto q_{1|t}(\mathbf{x}_1 | \mathbf{x}_t) \exp(-J(\mathbf{x}_1))$. This yields two estimator families:

$$\mathbf{g}_t^{\text{LGD}} = \frac{b_t\sigma_t^2}{\alpha_t} \mathbb{E}_{q_{1|t}^{(J)}(\mathbf{x}_1 | \mathbf{x}_t)} [\nabla_{\mathbf{x}_t} \log q_{1|t}(\mathbf{x}_1 | \mathbf{x}_t)], \quad (15)$$

$$\mathbf{g}_t^{\text{SIM}} = \frac{b_t\sigma_t^2}{\alpha_t} \mathbb{E}_{q_{1|t}^{(J)}(\mathbf{x}_1 | \mathbf{x}_t)} [\nabla_{\mathbf{x}_t} \log p_{1|t}(\mathbf{x}_1 | \mathbf{x}_t)]. \quad (16)$$

LGD replaces both the sampling distribution and the score with the proposal, whereas SIM replaces only the sampling distribution and retains the original score.

Theorem 2.1. Let $\epsilon^{(i)} \sim \mathcal{N}(\mathbf{0}, \mathbf{I})$ for $i = 1, \dots, n$, and $\mu(\mathbf{x}_t) \triangleq \mathbb{E}_{p_{1|t}(\mathbf{x}_1)}[\mathbf{x}_1] = -a_t\mathbf{x}_t/b_t + \mathbf{v}_t(\mathbf{x}_t)/b_t$. Different choices of $q_{1|t}$ yield different stochastic estimators of \mathbf{g}_t .

(i) **DPS.** For LGD, choosing a Dirac proposal $q_{1|t}(\mathbf{x}_1 | \mathbf{x}_t) = \delta(\mathbf{x}_1 - \mu(\mathbf{x}_t))$ gives (Chung et al., 2022)

$$\mathbf{g}_t^{\text{LGD-DPS}} = -b_t\sigma_t^2/\alpha_t \cdot \nabla_{\mathbf{x}_t} J(\mu(\mathbf{x}_t)). \quad (17)$$

(ii) **LGD-MC.** For LGD, choosing a Gaussian proposal $q_{1|t}(\mathbf{x}_1 | \mathbf{x}_t) = \mathcal{N}(\mu(\mathbf{x}_t), \Sigma_t)$ with $\Sigma_t = \mathbf{L}_t \mathbf{L}_t^\top$ and samples $\mathbf{x}_1^{(i)} = \mu(\mathbf{x}_t) + \mathbf{L}_t \epsilon^{(i)}$ yields (Song et al., 2023)

$$\mathbf{g}_t^{\text{LGD-MC}} = \frac{b_t\sigma_t^2}{\alpha_t} \nabla_{\mathbf{x}_t} \log \sum_{i=1}^n \frac{\exp(-J(\mathbf{x}_1^{(i)}))}{n}, \quad (18)$$

(iii) **SIM-MC.** For SIM, choosing a Gaussian proposal $q_{1|t}(\mathbf{x}_1 | \mathbf{x}_t) = \mathcal{N}(\mu(\mathbf{x}_t), \Sigma_t(\mathbf{x}_t))$ with $\Sigma_t(\mathbf{x}_t) = \mathbf{L}_t(\mathbf{x}_t) \mathbf{L}_t(\mathbf{x}_t)^\top$, defining $\mathbf{z}_t^{(i)} = \mathbf{L}_t(\mathbf{x}_t) \epsilon^{(i)}$, $\mathbf{x}_1^{(i)} = \mu(\mathbf{x}_t) + \mathbf{z}_t^{(i)}$, and $w_{\{\mathbf{x}_1^{(i)}\}}^{(J)}$ is computed as in Eq. 8. The Monte Carlo estimator in Feng et al. (2025) can be written as

$$\mathbf{g}_t^{\text{SIM-MC}} = b_t \sum_{i=1}^n w_{\{\mathbf{x}_1^{(i)}\}}^{(J)} \left(\mathbf{x}_1^{(i)} \right) \mathbf{z}_t^{(i)}, \quad (19)$$

The covariance $\Sigma_t(\mathbf{x}_t)$ depends on \mathbf{x}_t . But in LGD-MC, this dependence is typically ignored. SIM-MC assumes a fixed covariance for general tasks (Feng et al., 2025). The resulting approximation can qualitatively change the guidance. Fig. 1 (right) illustrates the differences in sampling behavior; circles/ellipses indicate the per-step variance.

The difference between $\mathbf{g}_t^{\text{LGD}}$ and $\mathbf{g}_t^{\text{SIM}}$ can be bounded in terms of how well the covariance is approximated.

Theorem 2.2. Let $q_{1|t}(\mathbf{x}_1) = \mathcal{N}(\mu(\mathbf{x}_t), \Sigma_t)$ and $q_t(\mathbf{z}_t) = \mathcal{N}(\mathbf{0}, \Sigma_t(\mathbf{x}_t))$. Define $J_t(\mathbf{z}_t) \triangleq J(\mu(\mathbf{x}_t) + \mathbf{z}_t)$, and $e_t(\mathbf{x}_t) \triangleq \left\| \Sigma_t - \sigma_t^2/\alpha_t \cdot \nabla_{\mathbf{x}_t} \mathbb{E}_{p_{1|t}(\mathbf{x}_1)}[\mathbf{x}_1] \right\|_2^2$. Then,

$$\|\mathbf{g}_t^{\text{LGD}} - \mathbf{g}_t^{\text{SIM}}\|_2^2 \leq b_t^2 \|\Sigma_t^{-1}\|_2^2 \mathbb{E}_{q_t^{(J_t)}(\mathbf{z}_t)} [\|\mathbf{z}_t\|_2^2] e_t(\mathbf{x}_t).$$

Actually, Boys et al. (2024) argues that an optimal Gaussian approximation should match both the mean and the variance, where the variance is

$$\Sigma_t(\mathbf{x}_t) = \mathbb{V}_{p_{1|t}(\mathbf{x}_1)}[\mathbf{x}_1] = \sigma_t^2/\alpha_t \cdot \nabla_{\mathbf{x}_t} \mathbb{E}_{p_{1|t}(\mathbf{x}_1)}[\mathbf{x}_1]. \quad (20)$$

However, in high-dimensional settings, this expression is difficult to use: forming the Jacobian is computationally expensive, and storing the resulting matrix is typically infeasible. In Boys et al. (2024), it is demonstrated only for

linear inverse problems with sparse operators. For more general settings, existing work does not provide a practical procedure for forming or approximating the required Jacobian (Boys et al., 2024; Feng et al., 2025).

2.5. Generation Method

Theorem 2.2 shows that SIM-style guidance requires the covariance $\Sigma_t(\mathbf{x}_t)$, which depends on the Jacobian $\nabla_{\mathbf{x}_t} \mathbb{E}_{p_{1|t}(\mathbf{x}_1|\mathbf{x}_t)}[\mathbf{x}_1]$. Explicitly forming this Jacobian is already expensive, and using it to construct $\Sigma_t(\mathbf{x}_t)$ and compute its matrix square root is even more infeasible. We therefore estimate the required quantities online from the sampler trajectory $\{(\mathbf{x}_k, \mathbf{v}_k)\}$ on a time grid $\{t_k\}$. Recall $\boldsymbol{\mu}(\mathbf{x}_t) \triangleq \mathbb{E}_{p_{1|t}(\mathbf{x}_1|\mathbf{x}_t)}[\mathbf{x}_1] = (\mathbf{v}_t(\mathbf{x}_t) - a_t \mathbf{x}_t) / b_t \Rightarrow \nabla_{\mathbf{x}_t} \mathbb{E}_{p_{1|t}(\mathbf{x}_1)}[\mathbf{x}_1] = -a_t \mathbf{I} / b_t + \nabla_{\mathbf{x}_t} \mathbf{v}_t(\mathbf{x}_t) / b_t$.

Theorem 2.3. Let $\mathbf{J}_k \approx \nabla_{\mathbf{x}_k} \mathbf{v}_{t_k}(\mathbf{x}_k)$ and define $\mathbf{B}_k = -a_{t_k} \mathbf{I} / b_{t_k} + \mathbf{J}_k / b_{t_k} \approx \nabla_{\mathbf{x}_k} \mathbb{E}_{p_{1|t}(\mathbf{x}_1)}[\mathbf{x}_1]$. Let $\mathbf{s}_k = \mathbf{x}_{k+1} - \mathbf{x}_k$, $\mathbf{r}_k = \mathbf{v}_{k+1} - \mathbf{v}_k$, and define $\mathbf{y}_k = -a_{t_k} \mathbf{s}_k / b_{t_k} + \mathbf{r}_k / b_{t_k}$. Further define $\rho_k = 1 / \mathbf{y}_k^\top \mathbf{s}_k$, $\mathbf{V}_k = \mathbf{I} - \rho_k \mathbf{s}_k \mathbf{y}_k^\top$, $u_k = b_{t_k} / b_{t_{k+1}}$, and $w_k = (a_{t_k} - a_{t_{k+1}}) / b_{t_{k+1}}$. Then the symmetric secant update admits the closed-form recursion:

$$\mathbf{B}_{k+1} = u_k (\mathbf{V}_k^\top \mathbf{B}_k \mathbf{V}_k + \rho_k \mathbf{y}_k \mathbf{y}_k^\top) + w_k \mathbf{I}. \quad (21)$$

Inspired by the compact representation of the DFP solution (Byrd et al., 1994), we initialize $\mathbf{B}_0 = \gamma \mathbf{I}$ and show that \mathbf{B}_k admits a compact form in general.

Theorem 2.4. \mathbf{B}_k admits the compact representation

$$\mathbf{B}_k = \gamma_k \mathbf{I} + \mathbf{U}_k \boldsymbol{\Gamma}_k \mathbf{U}_k^\top. \quad (22)$$

where, $\mathbf{U}_1 = [\mathbf{y}_0 \ \mathbf{s}_0]$, $\mathbf{U}_k = [\mathbf{U}_{k-1} \ \mathbf{s}_{k-1} \ \mathbf{y}_{k-1}]$. γ_k evolves by $\gamma_{k+1} = u_k \gamma_k + w_k$. Let $\mathbf{p}_k = \boldsymbol{\Gamma}_k \mathbf{U}_k^\top \mathbf{s}_k$, $\tau_k = \mathbf{s}_k^\top \mathbf{U}_k \boldsymbol{\Gamma}_k \mathbf{U}_k^\top \mathbf{s}_k$, and $\delta_k := \tau_k + \gamma_k \mathbf{s}_k^\top \mathbf{s}_k$. $\boldsymbol{\Gamma}_k$ satisfies the recursion

$$\boldsymbol{\Gamma}_{k+1} = u_k \begin{bmatrix} \boldsymbol{\Gamma}_k & \mathbf{0} & -\rho_k \mathbf{p}_k \\ \mathbf{0} & 0 & -\gamma_k \rho_k \\ -\rho_k \mathbf{p}_k^\top & -\gamma_k \rho_k & \rho_k (1 + \rho_k \delta_k) \end{bmatrix}, \quad (23)$$

This compact representation reveals the low-rank structure of the update increments, enabling a semi-numerical matrix square-root computation for the covariance at scale.

Theorem 2.5. Let $\mathbf{B} = \gamma \mathbf{I} + \mathbf{U} \mathbf{T} \mathbf{U}^\top$, $\gamma > 0$, where $\mathbf{U} \in \mathbb{R}^{d \times m}$ and $\boldsymbol{\Gamma} \in \mathbb{R}^{m \times m}$. Then \mathbf{B} admits a factorization $\mathbf{B} = \mathbf{L} \mathbf{L}^\top$ with $\mathbf{L} = \mathbf{Q} (\mathbf{L}_C - \sqrt{\gamma} \mathbf{I}) \mathbf{Q}^\top + \sqrt{\gamma} \mathbf{I}$, where (\mathbf{Q}, \mathbf{R}) is the reduced QR factorization of \mathbf{U} , and \mathbf{L}_C is the lower-triangular Cholesky factor of $\mathbf{C} = \gamma \mathbf{I} + \mathbf{R} \mathbf{F} \mathbf{R}^\top = \mathbf{L}_C \mathbf{L}_C^\top$.

In practice, following the notation in Theorem 2.3, to ensure the numerical stability of Theorem 2.5, we preserve the positive definiteness of \mathbf{B} by damping, replacing \mathbf{y}_k with

$$\hat{\mathbf{y}}_k = \varphi_k \mathbf{y}_k + (1 - \varphi_k) \mathbf{B}_k \mathbf{s}_k. \quad (24)$$

Algorithm 1 SA-MC (with memory queue)

Input: initial \mathbf{x}_0 ; time grid $\{t_k\}_{k=0}^K$; velocity field $\mathbf{v}_t(\mathbf{x})$; cost $J(\mathbf{x}_1)$; guide scale λ ; MC size S ; memory length m ; initial γ_0 ; schedules σ_t, α_t ; $a_t = \dot{\sigma}_t / \sigma_t$, $b_t = (\dot{\alpha}_t \sigma_t - \dot{\sigma}_t \alpha_t) / \sigma_t$. $\mathbf{U}_0 \leftarrow []$, $\boldsymbol{\Gamma}_0 \leftarrow []$, $\mathcal{M}_0 \leftarrow []$

Output: \mathbf{x}_K .

for $k = 0$ **to** $K - 1$ **do**

- $\mathbf{v}_k \leftarrow \mathbf{v}_{t_k}(\mathbf{x}_k)$
- if** $k \geq 1$ **then**

 - $(\mathbf{s}_{k-1}, \mathbf{r}_{k-1}) \leftarrow (\mathbf{x}_k - \mathbf{x}_{k-1}, \mathbf{v}_k - \mathbf{v}_{k-1})$
 - $(u_{k-1}, w_{k-1}) \leftarrow (b_{t_{k-1}} / b_{t_k}, (a_{t_{k-1}} - a_{t_k}) / b_{t_k})$
 - $\mathbf{y}_{k-1} \leftarrow -a_{t_{k-1}} \mathbf{s}_{k-1} / b_{t_{k-1}} + \mathbf{r}_{k-1} / b_{t_{k-1}}$
 - $\hat{\mathbf{y}}_{k-1} \leftarrow \text{DAMP.}(\mathbf{y}_{k-1}, \mathbf{s}_{k-1}, \gamma_{k-1}, \mathbf{U}_{k-1}, \boldsymbol{\Gamma}_{k-1})$
 - $\hat{\gamma}_{k-1} = \hat{\mathbf{y}}_{k-1}^\top \mathbf{s}_{k-1} / \mathbf{s}_{k-1}^\top \mathbf{s}_{k-1}$.
 - $\mathcal{M}_k \leftarrow \text{PUSH}(\mathcal{M}_{k-1}, (\mathbf{s}_{k-1}, \hat{\mathbf{y}}_{k-1}, u_{k-1}, w_{k-1}))$
 - $\mathcal{M}_k \leftarrow \text{POPOLDESTIFNEEDED}(\mathcal{M}_k, m)$
 - $(\gamma_k, \mathbf{U}_k, \boldsymbol{\Gamma}_k) \leftarrow \text{UPDATEB}(\mathcal{M}_k, \hat{\gamma}_{k-1})$

- end if**
- $\mathbf{x}_{1,k}^\text{pred} \leftarrow \mathbf{x}_k + (1 - t_k) \mathbf{v}_k$
- $\mathbf{L}_k \leftarrow \text{SEMINUMERICALSQRT}(\gamma_k, \mathbf{U}_k, \boldsymbol{\Gamma}_k)$
- $\mathbf{g}_k \leftarrow \text{SAMPLETILTEDMEAN}(\mathbf{x}_{1,k}^\text{pred}, \mathbf{L}_k, t_k, \lambda, J, S)$
- $\dot{\mathbf{x}}(t_k, \mathbf{x}_k) \leftarrow \mathbf{v}_k + b_{t_k} \mathbf{g}_k$
- $\mathbf{x}_{k+1} \leftarrow \text{ODESTEP}(\mathbf{x}_k, \dot{\mathbf{x}}(t_k, \mathbf{x}_k), t_k, t_{k+1})$

end for

return \mathbf{x}_K

The choice of φ_k and the rationale for preserving positive definiteness are discussed in App. C.2. Besides, we initialize γ_k in Theorem 2.4 by Jacobi-scale matching (Nocedal & Wright, 2006): $\hat{\gamma}^k = \mathbf{y}_k^\top \mathbf{s}_k / \mathbf{s}_k^\top \mathbf{s}_k$.

Finally, Eq. 23 implies that $\boldsymbol{\Gamma}_k \in \mathbb{R}^{2k \times 2k}$ grows with k . Since $\mathbf{v}_t(\mathbf{x})$ varies over time and space, retaining all past secant pairs is unnecessary. We therefore maintain a fixed-capacity queue of the most recent M entries:

$\mathcal{M}_k = ((\mathbf{s}_i, \hat{\mathbf{y}}_i, u_i, w_i))_{i=\max(0, k-M+1)}^k$. \mathbf{B}_{k+1} is computed using the information stored in \mathcal{M}_k .

3. Method

3.1. Optimization

Instantiation. We optimize in the Shape-VAE¹ latent space (Fig. 2a). Given a 3D geometry, we encode it to initialize latent \mathbf{x}_1 . We follow the time-annealed update in Eq. 12. At iteration k , we sample $t_k \sim \mathcal{U}(t_{\min}, t_{\max})$ and perturb the iterate as $\mathbf{x}_{t_k} = \text{ADDNOISE}(\mathbf{x}_k, t_k)$ using the flow noise schedule. Conditioned on the view, we get the score term with a DiT forward pass to obtain $\mathbf{v}_{t_k}(\mathbf{x}_{t_k})$. We instantiate $J(\cdot, \lambda)$ with a cost predictor and compute $\nabla_{\mathbf{x}_k} J(\mathbf{x}_k, \lambda)$ by automatic differentiation. After K steps, we decode \mathbf{x}_K to the optimized geometry; Alg. 2 summarizes the procedure.

¹The Shape-VAE and DiT in this paper use the open source weights released by Hunyuan3D 2.1 (Hunyuan3D et al., 2025).

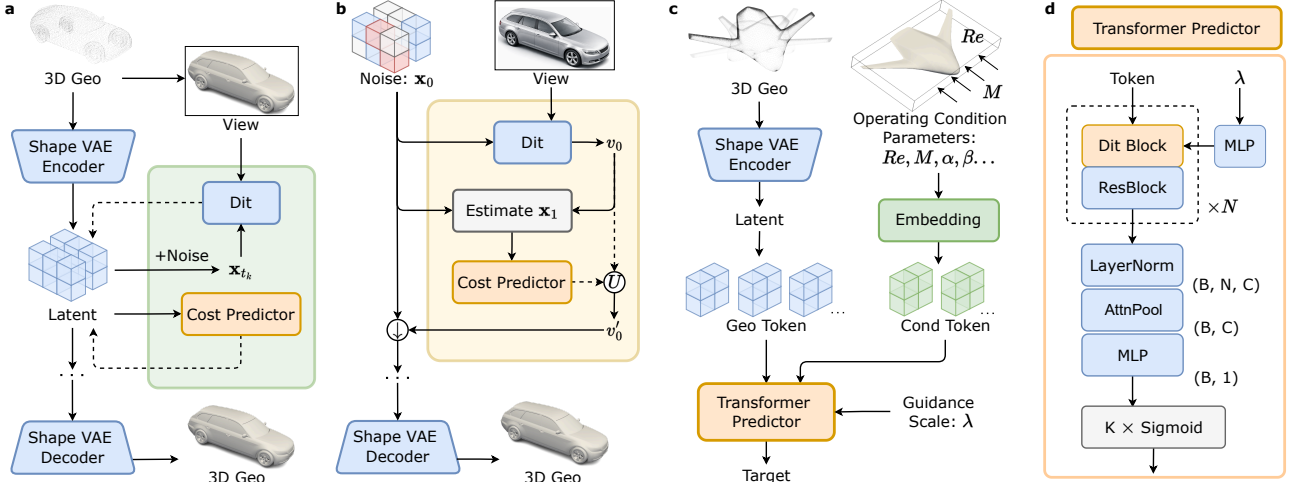


Figure 2. Method overview. **a**, Latent shape-preserving optimization in the Shape-VAE space. **b**, Guided flow-matching generation with a cost predictor. **c**, Cost predictor conditioned on geometry, operating conditions and λ . **d**, Detailed modules in Transformer predictor.

3.2. Generation

Instantiation As shown in Fig. 2b and Alg. 1, at step k we first query the DiT velocity field, $\mathbf{v}_k = \mathbf{v}_{t_k}(\mathbf{x}_k)$, and form the one-step prediction $\hat{\mathbf{x}}_1^k = \mathbf{x}_k + (1 - t_k)\mathbf{v}_k$. For $k \geq 1$, we update the Jacobian-induced matrix \mathbf{B}_k using the latest secant pair $(\mathbf{s}_{k-1}, \mathbf{r}_{k-1}) = (\mathbf{x}_k - \mathbf{x}_{k-1}, \mathbf{v}_k - \mathbf{v}_{k-1})$, together with the damped vector $\hat{\mathbf{y}}_{k-1}$ and a fixed-length memory queue. This yields the compact form $(\gamma_k, \mathbf{U}_k, \Gamma_k)$ and its factor $\mathbf{L}_k = \text{SEMINUMERICALSQRT}(\gamma_k, \mathbf{U}_k, \Gamma_k)$.

We then estimate the guidance term \mathbf{g}_k via SAMPLETILTEDMEAN, following Eq. 19. For $\mathbf{z}_k^{(i)} = \mathbf{L}_k(\mathbf{x}_k)\epsilon^{(i)}$ in Eq. 19, $\mathbf{L}_k(\mathbf{x}_k)\epsilon^{(i)}$ depends on \mathbf{x}_k ; SIM-MC treats $\mathbf{L}_k(\mathbf{x}_k)$ as a constant. In contrast, we estimate $\mathbf{L}_k(\mathbf{x}_k)\epsilon^{(i)}$ via $\mathbf{L}_k\epsilon^{(i)}$.

Finally, we modify the drift as $\dot{\mathbf{x}}(t_k, \mathbf{x}_k) = \mathbf{v}_k + \mathbf{g}_k$ and take one ODE step to obtain \mathbf{x}_{k+1} . After K steps, we decode \mathbf{x}_K to obtain the generated geometry.

Details of DAMP., UPDATEB, SEMINUMERICALSQRT, and SAMPLETILTEDMEAN are provided in Alg. 3, 4, 5, and 6.

Time Complexity. Let $C_{\text{DiT}}^{\text{fwd}}$ be the cost of one DiT forward pass and C_J^{fwd} the cost of one forward evaluation of the cost predictor. Let d be the latent dimension, m the memory length, and $r = 2m$ the rank of the compact secant form. Each step requires: (i) one DiT forward, $\mathcal{O}(C_{\text{DiT}}^{\text{fwd}})$; (ii) updating the low-rank secant structure (damping, queue update, UPDATEB), $\mathcal{O}(dr^2 + r^3)$; (iii) Monte Carlo guidance with S samples, including applying \mathbf{L}_k and S cost evaluations, $\mathcal{O}(S(dr + r^2) + S C_J^{\text{fwd}})$. Total K steps complexity is $\mathcal{O}(K[C_{\text{DiT}}^{\text{fwd}} + (dr^2 + r^3) + S(dr + r^2) + S C_J^{\text{fwd}}])$.

In practice, $r, S \ll d$, and $dr^2 + Sdr$ is essentially the cost of a single-layer, activation-free $\text{MLP}_{d \rightarrow (r^2 + Sr)}$ (latent). This overhead is typically negligible compared to the forward passes of the DiT model and the cost predictor.

3.3. Cost Predictor

As shown in Fig. 2c–d, we encode the 3D geometry with a Shape-VAE to obtain latent geometry tokens, and embed the operating conditions into condition tokens. We concatenate both token types and pass them to a Transformer predictor with N DiT blocks. Following Sec. 2.2, we condition the predictor on the guidance scale λ : a lightweight MLP maps λ to a modulation vector that is injected into each block via adaptive normalization. We then apply attention pooling and an MLP head to produce a scalar prediction. The model is trained with the minibatch objective in Eq. 8, using the λ -conditioned cost $J_\theta(\mathbf{x}, \lambda)$ in place of $\lambda J_\theta(\mathbf{x})$.

4. Experiments

4.1. Experimental Setup

We evaluate our method in two regimes: (i) a controlled 2D synthetic study that probes the theory, and (ii) 3D aerodynamic inverse design on high-fidelity CFD benchmarks.

2D experiment. We construct a 2D setting that mirrors the core ingredients of the 3D tasks: a base data distribution and a cost function. The data distribution is a Gaussian mixture, and the cost is a smooth random field generated by summing Gaussian RBFs. Full details are provided in App. E.1.

Dataset. We train on the vehicle dataset DrivAerNet++ (Elrefaeia et al., 2024) and the aircraft dataset BlendedNet (Sung et al., 2025). DrivAerNet++ provides diverse car geometries with high-fidelity CFD drag coefficients. BlendedNet provides diverse aircraft geometries with high-fidelity CFD lift and drag coefficients under varying operating conditions.

Evaluation. We evaluate both optimized and generated designs by running OpenFOAM simulations (Jasak et al., 2007). The computational domain, boundary conditions,

Table 1. Summary of car aerodynamic optimization baselines

PURE OPTIMIZATION		OPT. & GENERATION
SOURCE	COST GRADIENT	COST G. AND DPS
INSTANTIATIONS	TRAN ET AL. (2024) VATANI ET AL. (2025)	HAO ET AL. (2025) YOU ET AL. (2025)*

* No single-step estimation in DPS.

and meshing settings are described in App. F.1. In addition, we 3D-print the vehicles before/after optimization and those generated with/without guidance, and test them in a miniature wind tunnel. Wake size is assessed using multi-frame time-composited images; details are provided in App. F.3.

Baselines. For optimization, we denote methods that use only the cost gradient as cost gradient, and refer to our approach as density gradient. For generation, we compare with training-free baselines, including DPS (Chung et al., 2022), LGD-MC (Song et al., 2023), and SIM-MC (Feng et al., 2025). Existing car-shape optimization methods can be viewed as instantiations or variants of these schemes; we group them under these baselines, as summarized in Table 1.

4.2. 2D validation experiment.

Fig. 3a illustrates the setup: p is the data distribution and $cost$ defines the objective landscape. The target distribution q^* follows Eq. 4. Using the ground-truth cost gives q_{real} . Replacing it with a predictor trained on samples from p yields q_{MSE} (MSE training) and q_{SKL} (SKL training). Relative to q_{real} , q_{MSE} misses several modes, whereas q_{SKL} better preserves the target structure.

Fig. 3b visualizes guided generation. We visualize samples drawn from the data distribution p and the optimal distribution q_{real} . We first train a flow-matching model that maps noise to p (blue: noise; red: samples). We then guide sampling using (i) the ground-truth cost (REAL), (ii) an MSE-trained predictor, or (iii) an SKL-trained predictor. With the ground-truth cost, SA-MC best matches the spread of samples from q_{real} . With the MSE-trained predictor, samples show a consistent drift (toward the bottom-right) (analysis in App. G.1). In contrast, SA-MC combined with the SKL-trained predictor produces the closest match to q_{real} .

Fig. 3c compares cost-gradient and density-gradient optimization using predictors trained with MSE or SKL. Density-gradient optimization more reliably reaches the global optimum. Moreover, the MSE-trained predictor leads to solutions that deviate from the data distribution.

4.3. Vehicle aerodynamic optimization and generation.

In vehicle design, the drag coefficient (C_d) is the primary objective. We instantiate the cost predictor as a C_d predictor.

Optimization. Figs. 4a,b report quantitative results. Fig. 4a

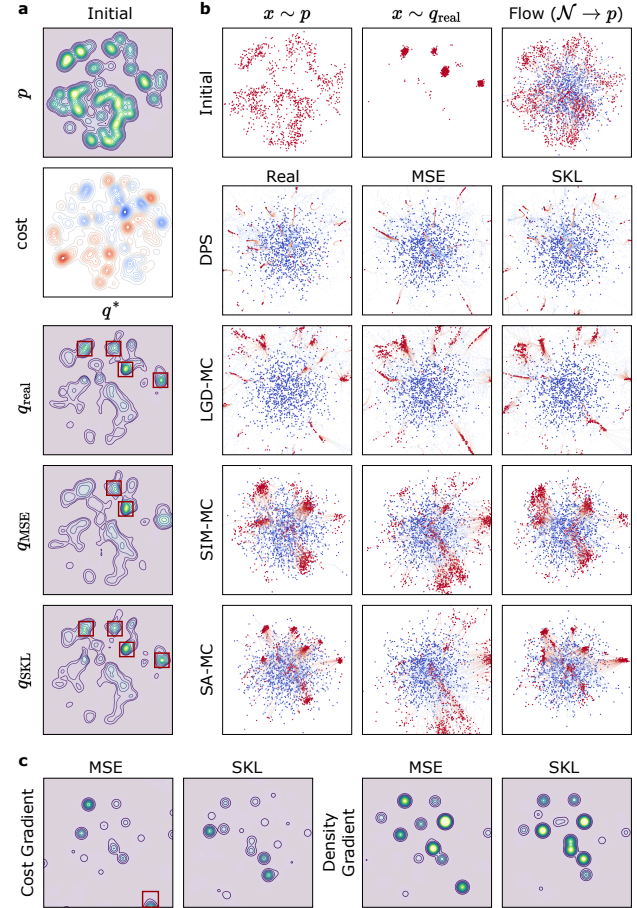


Figure 3. 2D validation experiment. a, Base distribution p , cost field, and target distributions (q^* (Eq. 4)) via ground-truth cost (q_{real}), cost predictors trained with MSE (q_{MSE}) and SKL (q_{SKL}). b, Flow matching from noise to p (blue: noise; red: samples) and guided sampling with DPS, LGD-MC, SIM-MC, and SA-MC using Real/MSE/SKL costs. c, Cost-gradient vs. density-gradient optimization using MSE- or SKL-trained cost predictors.

compares cost-gradient and density-gradient optimization using C_d predictors trained with either MSE or SKL. Density-gradient optimization consistently performs better, and SKL training provides more effective guidance than MSE. Fig. 4b evaluates shape preservation via Chamfer distance. We mark an empirical boundary beyond which optimized shapes often become implausible. Density-gradient optimization stays within this boundary more reliably, indicating improved shape preservation while reducing C_d . Fig. 4d shows OpenFOAM velocity fields for representative shapes. After optimization, the low-velocity wake region shrinks, and low-speed zones near the body are reduced. Fig. 4e reports a small wind-tunnel test on a 3D-printed example from (d), where the smoky wake becomes visibly smaller, consistent with reduced wake vortices.

Generation. Fig. 4c compares guided generation across guidance scales λ and training losses. With the SKL-trained predictor, SA-MC achieves the best overall performance,

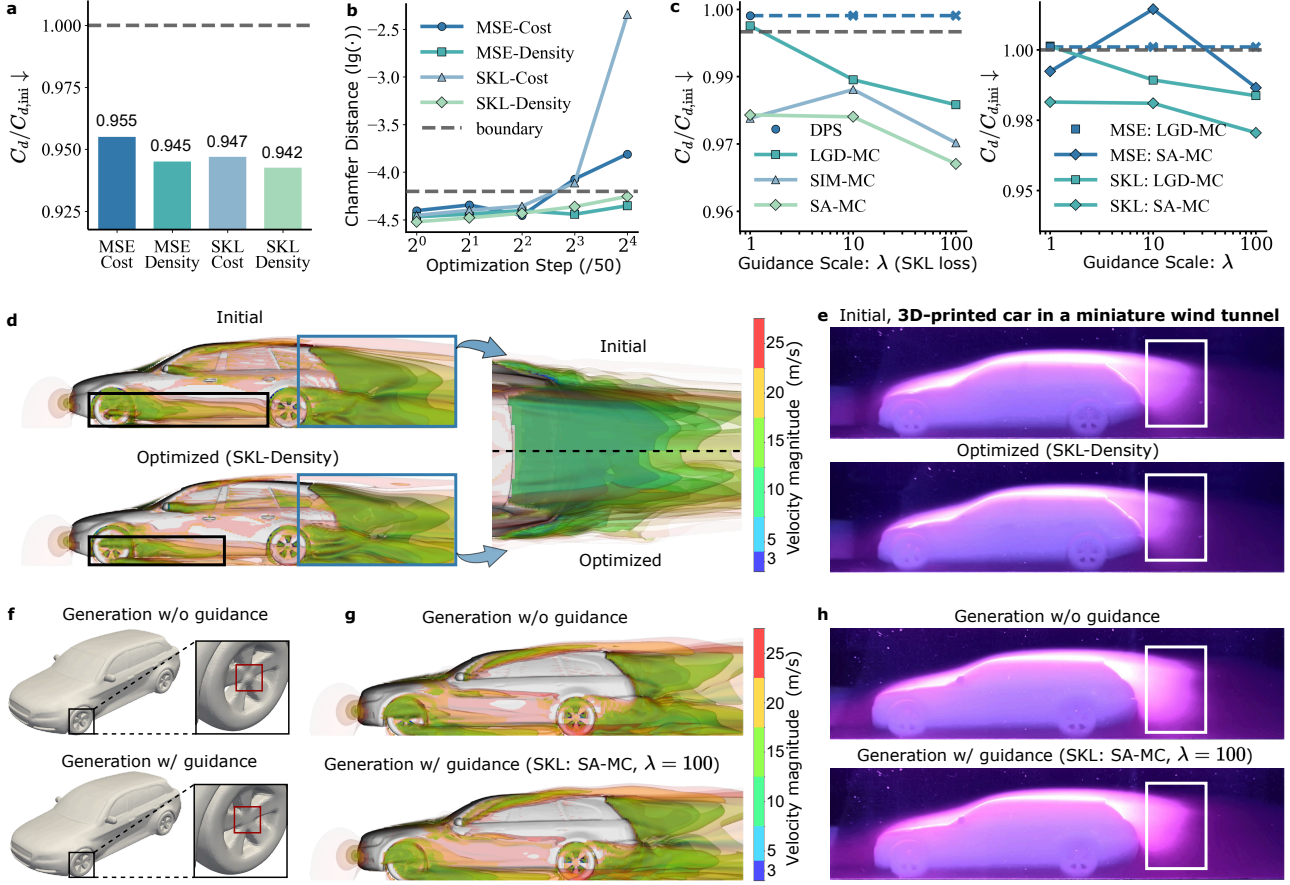


Figure 4. Vehicle aerodynamic optimization and generation. **a**, Drag reduction after optimization under different gradient and predictor training losses. **b**, Shape fidelity during optimization (Chamfer distance); dashed line marks an empirical plausibility boundary. **c**, Generation performance across guidance scales λ for different methods and training losses. **d**, OpenFOAM velocity magnitude before/after optimization, showing a reduced low-speed wake. **e**, Smoke visualization of 3D-printed shapes in a miniature wind tunnel, corroborating weaker wake turbulence after optimization. **f**, Example meshes generated without/with guidance. **g**, OpenFOAM velocity magnitude, SA-MC reduces low-speed wake. **h**, Wind-tunnel tests of 3D-printed SA-MC samples, which exhibit a similarly reduced turbulent region behind the vehicle.

while DPS fails to produce valid shapes at large λ . LGD-MC remains stable under the SKL-trained predictor across all tested λ , but under the MSE-trained predictor it succeeds only at $\lambda = 1$. Under MSE training, SA-MC at $\lambda = 10$ can even underperform the unguided baseline and yield higher C_d . All Monte Carlo-based methods use 32 samples, and the input view is the same. Fig. 4f visualizes samples with and without guidance, showing that guidance suppresses artifacts (abnormal protrusions on wheel). Fig. 4g compares OpenFOAM velocity magnitude, where SA-MC produces a smaller low-velocity wake. Finally, Fig. 4h shows wind-tunnel tests of 3D-printed SA-MC samples, which exhibit a similarly reduced turbulent region behind the vehicle.

4.4. Aircraft aerodynamic optimization and generation.

Aircraft design prioritizes the drag-to-lift ratio. We instantiate the cost predictor as a C_d/C_l (lift coefficient) predictor.

Optimization. Figs. 5a,b report quantitative results. In

Fig. 5a, the cost-gradient baseline drives lift to negative values, which is infeasible. In contrast, SKL-based density guidance achieves the largest improvement in C_d/C_l . Fig. 5b evaluates shape preservation: with more optimization steps, the cost-gradient method eventually violates the boundary constraint, whereas density guidance remains stable. Fig. 5e defines C_p -up and C_p -down as pressure distributions on the upper and lower wing surfaces; their difference is a proxy for lift. Qualitative examples are provided in Fig. 5f. Optimization removes low-speed residual regions near the wing and yields a smoother C_p distribution.

Generation. Fig. 5c reports generation results. To mirror practice, we select the best $\lambda \in \{1, 10, 100\}$ for each method. All Monte Carlo-based methods use 32 samples, and the input view is the same. SA-MC achieves the largest improvement, consistent with Fig. 5g, where it produces the highest-lift samples.

Time / Mem. Fig. 5d summarizes runtime and GPU mem-

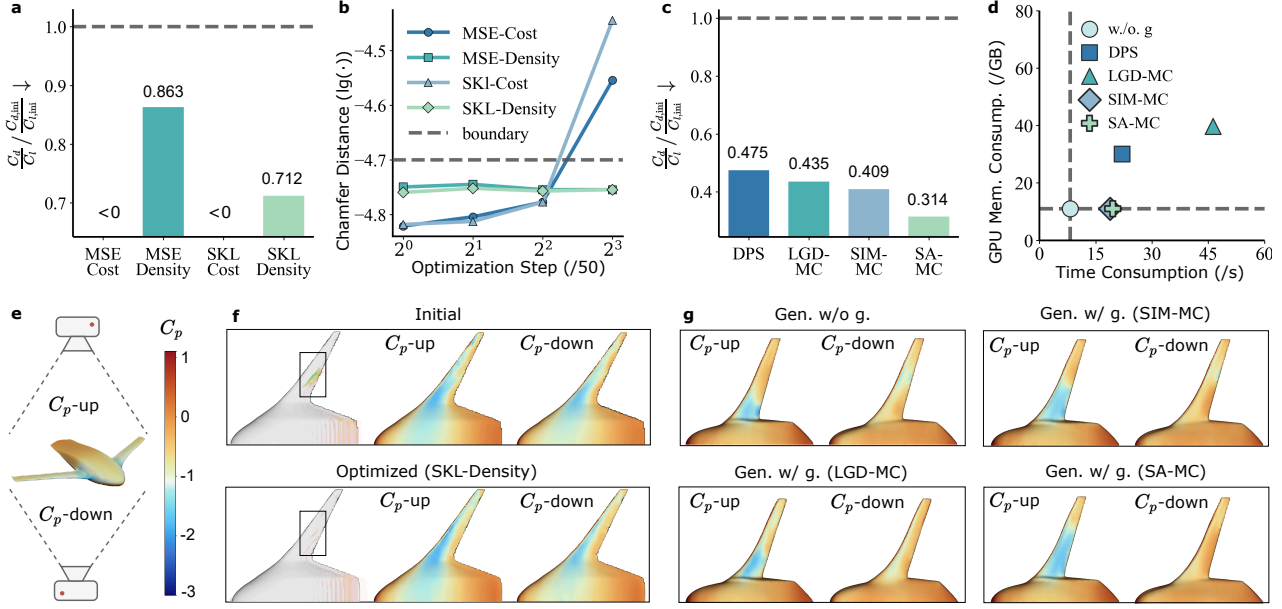


Figure 5. Aircraft aerodynamic optimization and generation. **a**, Optimized drag-to-lift ratio (C_d/C_l); cost-gradient guidance can yield negative lift (< 0). **b**, Shape fidelity during optimization (Chamfer distance); dashed line marks an empirical plausibility boundary. **c**, Best generated C_d/C_l over $\lambda \in \{1, 10, 100\}$ for each guidance method. **d**, Runtime and GPU memory for a single sample. **e**, Definition of $C_p and $C_pf, Velocity magnitude and Pressure before/after optimization, showing smoother C_p and reduced low-velocity region in the wake. **g**, Comparison of unguided and different guidance schemes; SA-MC yields lower C_p -up and higher C_p -down.$$

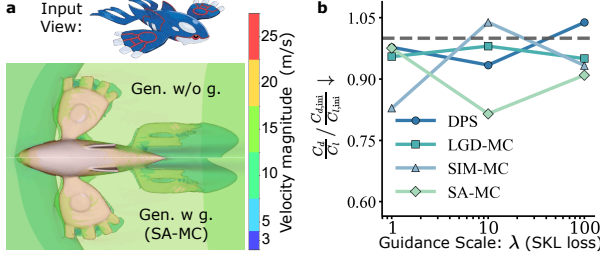


Figure 6. OOD Exp. (Kyogre). **a**, Input and OpenFOAM velocity magnitude (w/ and w/o guidance); SA-MC reduces the wake deficit. **b**, C_d/C_l versus guidance scale λ ; SA-MC performs best overall.

ory usage across guidance schemes. For a single sample, SA-MC is relatively fast; meanwhile, all methods finish within 1 minute. In terms of GPU memory, LGD-MC incurs substantially higher usage (> 40 GB), which can hinder practical deployment. SA-MC and SIM-MC exhibit memory footprints comparable to unguided generation.

OOD Experiments For the OOD setting, we test guided generation conditioned on Kyogre. For each generated mesh, we run OpenFOAM to compute the drag and lift coefficients. Fig. 6a shows the input image and the corresponding velocity magnitude visualization; SA-MC mitigates the low-velocity wake region. Fig. 6b compares methods across guidance scales. Possibly due to limited generalization, guided methods exhibit noticeable fluctuations. Nevertheless, SA-MC and LGD-MC achieve a better lift-to-drag ratio than the no-guidance baseline, while DPS and SIM-MC yield substantial gains at certain guidance scales. Overall,

SA-MC attains the lowest drag-to-lift ratio.

4.5. Offline Reinforcement Learning.

Due to the high cost of CFD evaluation, we instead use offline reinforcement learning to enable large-scale evaluation. Following the setup of Feng et al. (2025), we report results on offline reinforcement learning. SA-MC achieves the best average score among all methods (details in App. H).

5. Conclusions

We revisited inverse design through the lens of point and distributional solutions, linking them to shape-preserving optimization and guided generation. Based on this view, we proposed a divergence-based loss for training cost predictors and a density-gradient optimization scheme that leverages a learned data prior. We further unified existing guided-generation estimators and identified a key bottleneck: variance estimation for high-dimensional guidance. To address it, we introduced a time- and memory-efficient variance estimator. Experiments on a controlled 2D study and high fidelity 3D CFD benchmarks (vehicles and aircraft), validated by OpenFOAM simulations and miniature wind tunnel tests with 3D printed prototypes, together with offline RL results, demonstrate the effectiveness of our approach. **While guided generation has largely been explored in image editing, we hope this work will encourage its broader adoption in physics driven inverse design.**

Acknowledgments

The work is supported by the National Natural Science Foundation of China (No. 62276269 and No. 92270118) and the Beijing Natural Science Foundation (No. 1232009).

Author contributions

H.C., N.L., and L.C. jointly organized this project. H.C. and N.L. led the work on Sec. 2.1 and the experimental studies. N.L. led the work on Sec. 2.2–2.5 and was responsible for the theoretical proofs of the corresponding parts. L.C. provided support on the generative modeling components. H.S. supervised all aspects of the project. All authors participated in writing and revising the manuscript.

Impact Statement

This work contributes two complementary tools for physics-driven inverse design. First, it enables shape-preserving aerodynamic optimization directly on input meshes, improving objective values while maintaining plausible geometries. Second, it supports image-conditioned guided generation to produce diverse candidate shapes with improved aerodynamic metrics. These capabilities may support the design of vehicles and aircraft and help reduce reliance on expensive trial-and-error iterations in early-stage industrial workflows.

Most guided-generation research has focused on image editing. We hope this work encourages the use of guided generation as a new tool for physics-driven inverse design.

We do not expect this work to introduce immediate risks beyond the usual considerations for generative design systems. **Any generated or optimized design intended for real-world use should be validated with high-fidelity simulation and, when appropriate, physical testing, especially in safety-critical settings.**

References

- Anderson, J. D. *Aircraft performance and design*, volume 1221. McGraw-Hill New York, 1999.
- Bhatnagar, S., Afshar, Y., Pan, S., Duraisamy, K., and Kaushik, S. Prediction of aerodynamic flow fields using convolutional neural networks. *Computational Mechanics*, 64(2):525–545, 2019.
- Boys, B., Girolami, M., Pidstrigach, J., Reich, S., Mosca, A., and Akyildiz, O. D. Tweedie moment projected diffusions for inverse problems. *Transactions on Machine Learning Research*, 2024.
- Brunton, S. L., Noack, B. R., and Koumoutsakos, P. Machine learning for fluid mechanics. *Annual review of fluid mechanics*, 52(1):477–508, 2020.
- Byrd, R. H., Nocedal, J., and Schnabel, R. B. Representations of quasi-newton matrices and their use in limited memory methods. *Mathematical Programming*, 63(1):129–156, 1994.
- Chan, E. R., Lin, C. Z., Chan, M. A., Nagano, K., Pan, B., De Mello, S., Gallo, O., Guibas, L. J., Tremblay, J., Khamis, S., et al. Efficient geometry-aware 3d generative adversarial networks. In *Proceedings of the IEEE/CVF conference on computer vision and pattern recognition*, pp. 16123–16133, 2022.
- Choy, C. B., Xu, D., Gwak, J., Chen, K., and Savarese, S. 3d-r2n2: A unified approach for single and multi-view 3d object reconstruction. In *European conference on computer vision*, pp. 628–644. Springer, 2016.
- Chung, H., Kim, J., Mccann, M. T., Klasky, M. L., and Ye, J. C. Diffusion posterior sampling for general noisy inverse problems. *arXiv preprint arXiv:2209.14687*, 2022.
- Elrefaie, M., Morar, F., Dai, A., and Ahmed, F. Drivaernet++: A large-scale multimodal car dataset with computational fluid dynamics simulations and deep learning benchmarks. *Advances in Neural Information Processing Systems*, 37:499–536, 2024.
- Feng, R., Yu, C., Deng, W., Hu, P., and Wu, T. On the guidance of flow matching. *arXiv preprint arXiv:2502.02150*, 2025.
- Forrester, A. I. and Keane, A. J. Recent advances in surrogate-based optimization. *Progress in aerospace sciences*, 45(1-3):50–79, 2009.
- Fu, J., Kumar, A., Nachum, O., Tucker, G., and Levine, S. D4rl: Datasets for deep data-driven reinforcement learning. *arXiv preprint arXiv:2004.07219*, 2020.
- Giles, M. B. and Pierce, N. A. An introduction to the adjoint approach to design. *Flow, turbulence and combustion*, 65(3):393–415, 2000.
- Goodfellow, I., Pouget-Abadie, J., Mirza, M., Xu, B., Warde-Farley, D., Ozair, S., Courville, A., and Bengio, Y. Generative adversarial networks. *Communications of the ACM*, 63(11):139–144, 2020.
- Groueix, T., Fisher, M., Kim, V. G., Russell, B. C., and Aubry, M. A papier-mâché approach to learning 3d surface generation. In *Proceedings of the IEEE conference on computer vision and pattern recognition*, pp. 216–224, 2018.
- Hao, Y., Zhu, L., and Yang, Y. 3did: Direct 3d inverse design for aerodynamics with physics-aware optimization. In *The Thirty-ninth Annual Conference on Neural Information Processing Systems*, 2025.

- Ho, J., Jain, A., and Abbeel, P. Denoising diffusion probabilistic models. *Advances in neural information processing systems*, 33:6840–6851, 2020.
- Hucho, W.-H. *Aerodynamics of road vehicles: from fluid mechanics to vehicle engineering*. Elsevier, 2013.
- Hunyuan3D, T., Yang, S., Yang, M., Feng, Y., Huang, X., Zhang, S., He, Z., Luo, D., Liu, H., Zhao, Y., et al. Hunyuan3d 2.1: From images to high-fidelity 3d assets with production-ready pbr material. *arXiv preprint arXiv:2506.15442*, 2025.
- Jameson, A. and Martinelli, L. Aerodynamic shape optimization techniques based on control theory. In *Computational Mathematics Driven by Industrial Problems: Lectures given at the 1st Session of the Centro Internazionale Matematico Estivo (CIME) held in Martina Franca, Italy, June 21–27, 1999*, pp. 151–221. Springer, 2007.
- Janner, M., Du, Y., Tenenbaum, J. B., and Levine, S. Planning with diffusion for flexible behavior synthesis. *arXiv preprint arXiv:2205.09991*, 2022.
- Jasak, H., Jemcov, A., Tukovic, Z., et al. Openfoam: A c++ library for complex physics simulations. In *International workshop on coupled methods in numerical dynamics*, volume 1000, pp. 1–20. Dubrovnik, Croatia), 2007.
- Jun, H. and Nichol, A. Shap-e: Generating conditional 3d implicit functions. *arXiv preprint arXiv:2305.02463*, 2023.
- Kerbl, B., Kopanas, G., Leimkühler, T., and Drettakis, G. 3d gaussian splatting for real-time radiance field rendering. *ACM Transactions on Graphics*, 42(4), 2023.
- Kingma, D. P. and Welling, M. Auto-encoding variational bayes. *arXiv preprint arXiv:1312.6114*, 2013.
- Levine, S. Reinforcement learning and control as probabilistic inference: Tutorial and review. *arXiv preprint arXiv:1805.00909*, 2018.
- Li, Z., Kovachki, N., Azizzadenesheli, K., Liu, B., Bhattacharya, K., Stuart, A., and Anandkumar, A. Fourier neural operator for parametric partial differential equations. *arXiv preprint arXiv:2010.08895*, 2020.
- Lipman, Y., Chen, R. T., Ben-Hamu, H., Nickel, M., and Le, M. Flow matching for generative modeling. In *The Eleventh International Conference on Learning Representations*, 2023.
- Lipman, Y., Havasi, M., Holderrieth, P., Shaul, N., Le, M., Karrer, B., Chen, R. T., Lopez-Paz, D., Ben-Hamu, H., and Gat, I. Flow matching guide and code. *arXiv preprint arXiv:2412.06264*, 2024.
- Martins, J. R. Aerodynamic design optimization: Challenges and perspectives. *Computers & Fluids*, 239:105391, 2022.
- Mescheder, L., Oechsle, M., Niemeyer, M., Nowozin, S., and Geiger, A. Occupancy networks: Learning 3d reconstruction in function space. In *Proceedings of the IEEE/CVF conference on computer vision and pattern recognition*, pp. 4460–4470, 2019.
- Mildenhall, B., Srinivasan, P. P., Tancik, M., Barron, J. T., Ramamoorthi, R., and Ng, R. Nerf: Representing scenes as neural radiance fields for view synthesis. *Communications of the ACM*, 65(1):99–106, 2021.
- Nichol, A., Jun, H., Dhariwal, P., Mishkin, P., and Chen, M. Point-e: A system for generating 3d point clouds from complex prompts. *arXiv preprint arXiv:2212.08751*, 2022.
- Nocedal, J. and Wright, S. J. *Numerical optimization*. Springer, 2006.
- Park, J. J., Florence, P., Straub, J., Newcombe, R., and Lovegrove, S. Deep sdf: Learning continuous signed distance functions for shape representation. In *Proceedings of the IEEE/CVF conference on computer vision and pattern recognition*, pp. 165–174, 2019.
- Peng, S., Niemeyer, M., Mescheder, L., Pollefeys, M., and Geiger, A. Convolutional occupancy networks. In *European Conference on Computer Vision*, pp. 523–540. Springer, 2020.
- Powell, M. J. Algorithms for nonlinear constraints that use lagrangian functions. *Mathematical programming*, 14(1):224–248, 1978.
- Qi, C. R., Su, H., Mo, K., and Guibas, L. J. Pointnet: Deep learning on point sets for 3d classification and segmentation. In *Proceedings of the IEEE conference on computer vision and pattern recognition*, pp. 652–660, 2017.
- Queipo, N. V., Haftka, R. T., Shyy, W., Goel, T., Vaidyanathan, R., and Tucker, P. K. Surrogate-based analysis and optimization. *Progress in aerospace sciences*, 41(1):1–28, 2005.
- Rezende, D. and Mohamed, S. Variational inference with normalizing flows. In *International conference on machine learning*, pp. 1530–1538. PMLR, 2015.
- Riegler, G., Osman Ulusoy, A., and Geiger, A. Octnet: Learning deep 3d representations at high resolutions. In *Proceedings of the IEEE conference on computer vision and pattern recognition*, pp. 3577–3586, 2017.

- Smith, M. J., Potsdam, M., Wong, T.-C., Baeder, J. D., and Phanse, S. Evaluation of computational fluid dynamics to determine two-dimensional airfoil characteristics for rotorcraft applications. *Journal of the American Helicopter Society*, 51(1):70–79, 2006.
- Song, J., Zhang, Q., Yin, H., Mardani, M., Liu, M.-Y., Kautz, J., Chen, Y., and Vahdat, A. Loss-guided diffusion models for plug-and-play controllable generation. In *International Conference on Machine Learning*, pp. 32483–32498. PMLR, 2023.
- Song, Y., Sohl-Dickstein, J., Kingma, D. P., Kumar, A., Ermon, S., and Poole, B. Score-based generative modeling through stochastic differential equations. *arXiv preprint arXiv:2011.13456*, 2020.
- Sun, Y., Wang, Y., Liu, Z., Siegel, J., and Sarma, S. Pointgrow: Autoregressively learned point cloud generation with self-attention. In *Proceedings of the IEEE/CVF winter conference on applications of computer vision*, pp. 61–70, 2020.
- Sung, N., Spreizer, S., Elrefaie, M., Samuel, K., Jones, M. C., and Ahmed, F. Blendednet: A blended wing body aircraft dataset and surrogate model for aerodynamic predictions. In *International Design Engineering Technical Conferences and Computers and Information in Engineering Conference*, volume 89237, pp. V03BT03A049. American Society of Mechanical Engineers, 2025.
- Takikawa, T., Litalien, J., Yin, K., Kreis, K., Loop, C., Nowrouzezahrai, D., Jacobson, A., McGuire, M., and Fidler, S. Neural geometric level of detail: Real-time rendering with implicit 3d shapes. In *Proceedings of the IEEE/CVF conference on computer vision and pattern recognition*, pp. 11358–11367, 2021.
- Tarantola, A. *Inverse Problem Theory and Methods for Model Parameter Estimation*. Society for Industrial and Applied Mathematics, 2005. doi: 10.1137/1.9780898717921. URL <https://epubs.siam.org/doi/10.1137/1.9780898717921>.
- Tran, J., Fukami, K., Inada, K., Umehara, D., Ono, Y., Ogawa, K., and Taira, K. Aerodynamics-guided machine learning for design optimization of electric vehicles. *Communications Engineering*, 3(1):174, 2024.
- Vatani, P., Elrefaie, M., Nazarpour, F., and Ahmed, F. Trioptimizer: Generative 3d shape optimization and drag prediction using triplane vae networks. *arXiv preprint arXiv:2509.12224*, 2025.
- Wang, N., Zhang, Y., Li, Z., Fu, Y., Liu, W., and Jiang, Y.-G. Pixel2mesh: Generating 3d mesh models from single rgb images. In *Proceedings of the European conference on computer vision (ECCV)*, pp. 52–67, 2018.
- Wang, Z., Lu, C., Wang, Y., Bao, F., Li, C., Su, H., and Zhu, J. Prolificdreamer: High-fidelity and diverse text-to-3d generation with variational score distillation. *Advances in neural information processing systems*, 36:8406–8441, 2023.
- Wu, H., Luo, H., Wang, H., Wang, J., and Long, M. Transolver: A fast transformer solver for pdes on general geometries. *arXiv preprint arXiv:2402.02366*, 2024.
- Wu, J., Zhang, C., Xue, T., Freeman, B., and Tenenbaum, J. Learning a probabilistic latent space of object shapes via 3d generative-adversarial modeling. *Advances in neural information processing systems*, 29, 2016.
- Wu, Z., Song, S., Khosla, A., Yu, F., Zhang, L., Tang, X., and Xiao, J. 3d shapenets: A deep representation for volumetric shapes. In *Proceedings of the IEEE conference on computer vision and pattern recognition*, pp. 1912–1920, 2015.
- Xiang, J., Chen, X., Xu, S., Wang, R., Lv, Z., Deng, Y., Zhu, H., Dong, Y., Zhao, H., Yuan, N. J., et al. Native and compact structured latents for 3d generation. *arXiv preprint arXiv:2512.14692*, 2025a.
- Xiang, J., Lv, Z., Xu, S., Deng, Y., Wang, R., Zhang, B., Chen, D., Tong, X., and Yang, J. Structured 3d latents for scalable and versatile 3d generation. In *Proceedings of the Computer Vision and Pattern Recognition Conference*, pp. 21469–21480, 2025b.
- Yang, G., Huang, X., Hao, Z., Liu, M.-Y., Belongie, S., and Hariharan, B. Pointflow: 3d point cloud generation with continuous normalizing flows. In *Proceedings of the IEEE/CVF international conference on computer vision*, pp. 4541–4550, 2019.
- You, Y., Zhao, C., Zhang, H., Xu, M., and Fua, P. Physgen: Physically grounded 3d shape generation for industrial design. *arXiv preprint arXiv:2512.00422*, 2025.
- Zhao, Z., Lai, Z., Lin, Q., Zhao, Y., Liu, H., Yang, S., Feng, Y., Yang, M., Zhang, S., Yang, X., et al. Hunyuan3d 2.0: Scaling diffusion models for high resolution textured 3d assets generation. *arXiv preprint arXiv:2501.12202*, 2025.

Contents of Appendix

A Related Work	13
B Proof	15
B.1 Proof of Theorem 2.1	15
B.2 Proof of Theorem 2.2	17
B.3 Proof of Theorem 2.3	18
B.4 Proof of Theorem 2.4	19
B.5 Proof of Theorem 2.5	20
C Additional Analysis of Theorem	21
C.1 Relationship between $\mathcal{J}_{\text{SKL}}^{(\lambda)}$ and the MSE Loss	21
C.2 The choice of φ_k and the rationale for preserving positive definiteness	23
D Algorithms and time-complexity analysis.	25
D.1 Time-annealed optimization	25
D.2 Damping (Damp.) algorithm	25
D.3 UpdataB algorithm	26
D.4 SemiNumericalSqrt algorithm	27
D.5 SampleTiltedMean algorithm	27
E Experiment Setting	29
E.1 2D Experimental Setting	29
E.2 Vehicle aerodynamic optimization and generation setting	29
E.3 Aircraft aerodynamic optimization and generation setting	30
F Evaluation	31
F.1 DrivAer Car OpenFOAM Setting	31
F.2 Blender OpenFOAM Setting	32
F.3 3D-printed car and miniature wind tunnel testing	32
G Additional Analysis of Experiment Results	35
G.1 Why do guided methods with an MSE-trained predictor exhibit a consistent drift?	35
H Offline Reinforcement Learning	36
H.1 Experiment Setting	36
H.2 Result and analysis	36

A. Related Work

Designing aerodynamically high-performing shapes is a challenging yet practically important inverse problem. Motivated by the limitations of existing data-driven approaches discussed above, this section reviews three research directions that underpin our proposed framework: aerodynamic shape optimization and surrogate modeling, 3D geometric representations and generative models, and sampling and optimization strategies in generative modeling.

Aerodynamic shape optimization and surrogate models. Traditional aerodynamic shape optimization is commonly cast as a PDE-constrained problem by coupling CFD solvers with numerical optimization and iterative geometry/mesh updates (Jameson & Martinelli, 2007; Martins, 2022). Gradient-based methods, especially adjoint approaches, scale well with the number of design variables, yet still require many expensive flow solutions, making broad design-space exploration costly (Giles & Pierce, 2000). This motivates surrogate-based analysis and optimization, where regression models (e.g., response surfaces or Kriging/GP) reduce the reliance on high-fidelity CFD evaluations (Queipo et al., 2005; Forrester & Keane, 2009).

More recently, deep learning surrogates have shown strong capability in learning nonlinear mappings from geometry and operating conditions to flow fields or integral coefficients, enabling rapid evaluation (Brunton et al., 2020; Bhatnagar et al., 2019; Li et al., 2020; Wu et al., 2024).

In recent years, deep learning-based approaches to aerodynamic optimization have rapidly proliferated. Tran et al. (2024) proposed an autoencoder that jointly learns geometry reconstruction and drag prediction, enabling car-shape optimization in latent space. Vatani et al. (2025) improved geometric fidelity with a triplane VAE and optimized shapes by partially fine-tuning the model. Hao et al. (2025) incorporated 3D diffusion models to expand beyond the training distribution. You et al. (2025) trained a flow-matching generative model and introduced SDF based mesh generation.

3D geometric representations and generative models. Modern 3D generative modeling is inextricably linked to the choice of geometric representation. Early approaches often adopt dense voxel or occupancy grids due to their conceptual simplicity; however, their memory and computational requirements grow cubically with resolution, motivating the development of sparse or hierarchical designs, such as octree-based convolutions (Wu et al., 2015; Choy et al., 2016; Riegler et al., 2017). Surface-based discretizations provide compact alternatives. Point clouds are lightweight but do not explicitly encode connectivity or watertightness, while meshes are directly usable in downstream simulation and CAD workflows but remain difficult to generate robustly due to topology and quality constraints (Qi et al., 2017; Wang et al., 2018; Groueix et al., 2018). In contrast, implicit continuous representations, especially occupancy fields and signed distance functions (SDFs), define geometry as the level set of a scalar field, naturally support resolution-independent detail and flexible topology (Mescheder et al., 2019; Park et al., 2019). Moreover, modern differentiable 3D representations, including neural radiance fields (NeRF) and 3D Gaussian splatting (3DGS), are increasingly integrated into hybrid pipelines to facilitate efficient rendering and supervision (Mildenhall et al., 2021; Kerbl et al., 2023). To further improve efficiency and high-frequency fidelity, many recent systems first synthesize structured intermediate feature fields, for example, plane, triplane-based grids, or multi-resolution feature volumes, and then decode them with lightweight implicit heads to answer occupancy or SDF queries (Peng et al., 2020; Chan et al., 2022; Takikawa et al., 2021). To learn the distributions of these representations, diverse generative families including VAEs, GANs, autoregressive Transformers, normalizing flows, and diffusion models have been employed to model 3D shape distributions, either directly in representation space or via latent feature fields (Kingma & Welling, 2013; Goodfellow et al., 2020; Wu et al., 2016; Sun et al., 2020; Rezende & Mohamed, 2015; Yang et al., 2019; Ho et al., 2020; Song et al., 2020; Nichol et al., 2022; Jun & Nichol, 2023). Recent large-scale 3D asset generators, such as Hunyuan3D series (Zhao et al., 2025; Hunyuan3D et al., 2025) and TRELLIS series (Xiang et al., 2025b;a), employ VAE to compress geometry into compact latent feature fields, and subsequently utilize diffusion models as the generative prior, enabling high-fidelity geometric synthesis with scalable compute.

Guided generation. As discussed in Sec. 2.1, once we train a generative model that maps a simple noise distribution to the data distribution, sampling from the *distributional* solution of an inverse-design problem corresponds to guidance-based generation. DPS enforces measurement consistency by injecting gradient terms along the diffusion trajectory (Chung et al., 2022). LGD-MC further alleviates systematic guidance bias through Monte Carlo approximations (Song et al., 2023). More recently, Feng et al. (2025) generalized these ideas to flow matching, providing a unified formulation for guidance under general probability paths, in which diffusion guidance methods such as DPS and LGD arise as special cases. The same framework also introduces SIM-MC, which approximates the required gradients using a predictor’s forward pass, substantially reducing computational cost (Feng et al., 2025).

Despite their practical success, existing guidance estimators share a common limitation. From the perspective of optimal Gaussian approximations, an ideal conditional approximation should match *both* the conditional mean and covariance (Boys et al., 2024). However, most existing methods either ignore the covariance term altogether or treat it as a fixed heuristic, which can lead to suboptimal. Moreover, the available theoretical justification for covariance matching is currently established only in restricted cases, such as linear inverse problems with sparse operators (Boys et al., 2024). For more general nonlinear objectives and high-dimensional generators, prior work does not provide a practical procedure to form, store, or approximate the required Jacobian (and hence the conditional covariance) at scale.

B. Proof

B.1. Proof of Theorem 2.1

Proof. We derive each estimator by specifying the proposal $q_{1|t}(\mathbf{x}_1 | \mathbf{x}_t)$ in the LGD and SIM formulations. Let $\boldsymbol{\epsilon}^{(i)} \sim \mathcal{N}(\mathbf{0}, \mathbf{I})$, and recall the conditional mean

$$\boldsymbol{\mu}(\mathbf{x}_t) \triangleq \mathbb{E}_{p_{1|t}(\mathbf{x}_1 | \mathbf{x}_t)}[\mathbf{x}_1] = -\frac{a_t}{b_t} \mathbf{x}_t + \frac{1}{b_t} \mathbf{v}_t(\mathbf{x}_t). \quad (25)$$

LGD (DPS and LGD-MC). Define the log-partition function

$$Z_t(\mathbf{x}_t) \triangleq \mathbb{E}_{q_{1|t}(\mathbf{x}_1 | \mathbf{x}_t)}[\exp(-J(\mathbf{x}_1))] = \int q_{1|t}(\mathbf{x}_1 | \mathbf{x}_t) \exp(-J(\mathbf{x}_1)) d\mathbf{x}_1. \quad (26)$$

Then

$$\nabla_{\mathbf{x}_t} \log Z_t(\mathbf{x}_t) = \frac{1}{Z_t(\mathbf{x}_t)} \nabla_{\mathbf{x}_t} Z_t(\mathbf{x}_t). \quad (27)$$

Under mild regularity conditions that allow exchanging differentiation and integration, differentiating under the integral sign gives

$$\begin{aligned} \nabla_{\mathbf{x}_t} Z_t(\mathbf{x}_t) &= \int \exp(-J(\mathbf{x}_1)) \nabla_{\mathbf{x}_t} q_{1|t}(\mathbf{x}_1 | \mathbf{x}_t) d\mathbf{x}_1 \\ &= \int q_{1|t}(\mathbf{x}_1 | \mathbf{x}_t) \exp(-J(\mathbf{x}_1)) \nabla_{\mathbf{x}_t} \log q_{1|t}(\mathbf{x}_1 | \mathbf{x}_t) d\mathbf{x}_1. \end{aligned} \quad (28)$$

Introduce the exponentially tilted distribution

$$q_{1|t}^{(J)}(\mathbf{x}_1 | \mathbf{x}_t) \triangleq \frac{q_{1|t}(\mathbf{x}_1 | \mathbf{x}_t) \exp(-J(\mathbf{x}_1))}{Z_t(\mathbf{x}_t)}. \quad (29)$$

Substituting into the gradient of $\log Z_t$ yields the identity

$$\nabla_{\mathbf{x}_t} \log Z_t(\mathbf{x}_t) = \mathbb{E}_{q_{1|t}^{(J)}(\mathbf{x}_1 | \mathbf{x}_t)}[\nabla_{\mathbf{x}_t} \log q_{1|t}(\mathbf{x}_1 | \mathbf{x}_t)]. \quad (30)$$

Therefore the LGD guidance direction can be written as

$$\mathbf{g}_t^{\text{LGD}} = \frac{b_t \sigma_t^2}{\alpha_t} \nabla_{\mathbf{x}_t} \log \mathbb{E}_{q_{1|t}(\mathbf{x}_1 | \mathbf{x}_t)}[\exp(-J(\mathbf{x}_1))]. \quad (31)$$

When $q_{1|t}(\cdot | \mathbf{x}_t)$ is reparameterizable, i.e., $\mathbf{x}_1 = \mathcal{T}(\mathbf{x}_t, \boldsymbol{\epsilon})$ with $\boldsymbol{\epsilon} \sim \mathcal{N}(\mathbf{0}, \mathbf{I})$, we have

$$Z_t(\mathbf{x}_t) = \mathbb{E}_{\boldsymbol{\epsilon}}[\exp(-J(\mathcal{T}(\mathbf{x}_t, \boldsymbol{\epsilon})))]. \quad (32)$$

A practical Monte Carlo estimator is obtained by drawing $\boldsymbol{\epsilon}^{(i)}$ and setting $\mathbf{x}_1^{(i)} = \mathcal{T}(\mathbf{x}_t, \boldsymbol{\epsilon}^{(i)})$, which gives

$$\mathbf{g}_t^{\text{LGD}} \approx \frac{b_t \sigma_t^2}{\alpha_t} \nabla_{\mathbf{x}_t} \log \left(\frac{1}{n} \sum_{i=1}^n \exp(-J(\mathbf{x}_1^{(i)})) \right). \quad (33)$$

In particular, if $q_{1|t}(\mathbf{x}_1 | \mathbf{x}_t) = \delta(\mathbf{x}_1 - \boldsymbol{\mu}(\mathbf{x}_t))$, then

$$\mathbf{g}_t^{\text{LGD-DPS}} = -\frac{b_t \sigma_t^2}{\alpha_t} \nabla_{\mathbf{x}_t} J(\boldsymbol{\mu}(\mathbf{x}_t)), \quad (34)$$

and if $q_{1|t}(\mathbf{x}_1 | \mathbf{x}_t) = \mathcal{N}(\boldsymbol{\mu}(\mathbf{x}_t), \boldsymbol{\Sigma}_t)$ with $\boldsymbol{\Sigma}_t = \mathbf{L}_t \mathbf{L}_t^\top$, then using $\mathbf{x}_1^{(i)} = \boldsymbol{\mu}(\mathbf{x}_t) + \mathbf{L}_t \boldsymbol{\epsilon}^{(i)}$ yields

$$\mathbf{g}_t^{\text{LGD-MC}} = \frac{b_t \sigma_t^2}{\alpha_t} \nabla_{\mathbf{x}_t} \log \left(\frac{1}{n} \sum_{i=1}^n \exp(-J(\mathbf{x}_1^{(i)})) \right). \quad (35)$$

SIM (SIM-MC). Start from the SIM estimator in score form (Eq. 14 in the main text):

$$\mathbf{g}_t^{\text{SIM}} = \frac{b_t \sigma_t^2}{\alpha_t} \mathbb{E}_{q_{1|t}^{(J)}(\mathbf{x}_1 | \mathbf{x}_t)} [\nabla_{\mathbf{x}_t} \log p_{1|t}(\mathbf{x}_1 | \mathbf{x}_t)], \quad (36)$$

where $q_{1|t}^{(J)}(\mathbf{x}_1 | \mathbf{x}_t) \propto q_{1|t}(\mathbf{x}_1 | \mathbf{x}_t) \exp(-J(\mathbf{x}_1))$. We will use the identity

$$\mathbb{E}_{q_{1|t}(\mathbf{x}_1 | \mathbf{x}_t)} [\nabla_{\mathbf{x}_t} \log p_{1|t}(\mathbf{x}_1 | \mathbf{x}_t)] = \mathbf{0}. \quad (37)$$

To verify equation 37, apply Bayes' rule:

$$\nabla_{\mathbf{x}_t} \log p_{1|t}(\mathbf{x}_1 | \mathbf{x}_t) = \nabla_{\mathbf{x}_t} \log p_{t|1}(\mathbf{x}_t | \mathbf{x}_1) - \nabla_{\mathbf{x}_t} \log p_t(\mathbf{x}_t). \quad (38)$$

For the forward noising kernel $p_{t|1}(\mathbf{x}_t | \mathbf{x}_1) = \mathcal{N}(\alpha_t \mathbf{x}_1, \sigma_t^2 \mathbf{I})$, we have

$$\nabla_{\mathbf{x}_t} \log p_{t|1}(\mathbf{x}_t | \mathbf{x}_1) = \frac{1}{\sigma_t^2} (\alpha_t \mathbf{x}_1 - \mathbf{x}_t). \quad (39)$$

Taking expectation under $q_{1|t}(\mathbf{x}_1 | \mathbf{x}_t)$ yields

$$\mathbb{E}_{q_{1|t}} [\nabla_{\mathbf{x}_t} \log p_{1|t}(\mathbf{x}_1 | \mathbf{x}_t)] = \frac{1}{\sigma_t^2} (\alpha_t \mathbb{E}_{q_{1|t}} [\mathbf{x}_1] - \mathbf{x}_t) - \nabla_{\mathbf{x}_t} \log p_t(\mathbf{x}_t). \quad (40)$$

We choose the SIM proposal to match the conditional mean, $q_{1|t}(\mathbf{x}_1 | \mathbf{x}_t) = \mathcal{N}(\boldsymbol{\mu}(\mathbf{x}_t), \boldsymbol{\Sigma}_t(\mathbf{x}_t))$, so that $\mathbb{E}_{q_{1|t}} [\mathbf{x}_1] = \boldsymbol{\mu}(\mathbf{x}_t)$. By the (Tweedie) identity implied by the definition of $\boldsymbol{\mu}(\mathbf{x}_t)$,

$$\nabla_{\mathbf{x}_t} \log p_t(\mathbf{x}_t) = \frac{1}{\sigma_t^2} (\alpha_t \boldsymbol{\mu}(\mathbf{x}_t) - \mathbf{x}_t), \quad (41)$$

and substituting into equation 40 gives equation 37.

Using equation 37, we can subtract zero from equation 36:

$$\mathbf{g}_t^{\text{SIM}} = \frac{b_t \sigma_t^2}{\alpha_t} \left(\mathbb{E}_{q_{1|t}^{(J)}} [\nabla_{\mathbf{x}_t} \log p_{1|t}(\mathbf{x}_1 | \mathbf{x}_t)] - \mathbb{E}_{q_{1|t}} [\nabla_{\mathbf{x}_t} \log p_{1|t}(\mathbf{x}_1 | \mathbf{x}_t)] \right). \quad (42)$$

Plugging in the Bayes decomposition and canceling the $\nabla_{\mathbf{x}_t} \log p_t(\mathbf{x}_t)$ term yields

$$\begin{aligned} \mathbf{g}_t^{\text{SIM}} &= \frac{b_t \sigma_t^2}{\alpha_t} \left(\mathbb{E}_{q_{1|t}^{(J)}} [\nabla_{\mathbf{x}_t} \log p_{t|1}(\mathbf{x}_t | \mathbf{x}_1)] - \mathbb{E}_{q_{1|t}} [\nabla_{\mathbf{x}_t} \log p_{t|1}(\mathbf{x}_t | \mathbf{x}_1)] \right) \\ &= \frac{b_t \sigma_t^2}{\alpha_t} \cdot \frac{\alpha_t}{\sigma_t^2} \left(\mathbb{E}_{q_{1|t}^{(J)}} [\mathbf{x}_1] - \mathbb{E}_{q_{1|t}} [\mathbf{x}_1] \right) = b_t \left(\mathbb{E}_{q_{1|t}^{(J)}} [\mathbf{x}_1] - \boldsymbol{\mu}(\mathbf{x}_t) \right). \end{aligned} \quad (43)$$

Finally, write $\mathbf{x}_1 = \boldsymbol{\mu}(\mathbf{x}_t) + \mathbf{z}_t$ with $q_t(\mathbf{z}_t) = \mathcal{N}(\mathbf{0}, \boldsymbol{\Sigma}_t(\mathbf{x}_t))$ and define $J_t(\mathbf{z}_t) \triangleq J(\boldsymbol{\mu}(\mathbf{x}_t) + \mathbf{z}_t)$. Then equation 43 becomes

$$\mathbf{g}_t^{\text{SIM}} = b_t \mathbb{E}_{q_t^{(J_t)}} [\mathbf{z}_t] = b_t \mathbb{E}_{q_t} \left[w^{(J)}(\boldsymbol{\mu}(\mathbf{x}_t) + \mathbf{z}_t) \mathbf{z}_t \right], \quad (44)$$

where $q_t^{(J_t)}(\mathbf{z}_t) \propto q_t(\mathbf{z}_t) \exp(-J_t(\mathbf{z}_t))$ and $w^{(J)}$ is the corresponding normalized weight. Sampling $\mathbf{z}_t^{(i)} = \mathbf{L}_t(\mathbf{x}_t) \boldsymbol{\epsilon}^{(i)}$ and setting $\mathbf{x}_1^{(i)} = \boldsymbol{\mu}(\mathbf{x}_t) + \mathbf{z}_t^{(i)}$, the Monte Carlo approximation gives

$$\mathbf{g}_t^{\text{SIM-MC}} = b_t \sum_{i=1}^n w_{\{\mathbf{x}_1^{(i)}\}}^{(J)} \left(\mathbf{x}_1^{(i)} \right) \mathbf{z}_t^{(i)}, \quad (45)$$

where $w_{\{\mathbf{x}_1^{(i)}\}}^{(J)}$ is the normalized exponential weight over the n samples (Eq. 8 in the main text). \square

B.2. Proof of Theorem 2.2

Proof. Fix \mathbf{x}_t throughout and write $\boldsymbol{\mu} = \boldsymbol{\mu}(\mathbf{x}_t)$. Starting from the score-based definitions under a proposal $q_{1|t}$,

$$\mathbf{g}_t^{\text{LGD}} = \frac{b_t \sigma_t^2}{\alpha_t} \mathbb{E}_{q_{1|t}^{(J)}(\mathbf{x}_1 | \mathbf{x}_t)} [\nabla_{\mathbf{x}_t} \log q_{1|t}(\mathbf{x}_1 | \mathbf{x}_t)], \quad \mathbf{g}_t^{\text{SIM}} = \frac{b_t \sigma_t^2}{\alpha_t} \mathbb{E}_{q_{1|t}^{(J)}(\mathbf{x}_1 | \mathbf{x}_t)} [\nabla_{\mathbf{x}_t} \log p_{1|t}(\mathbf{x}_1 | \mathbf{x}_t)], \quad (46)$$

where $q_{1|t}^{(J)}(\mathbf{x}_1 | \mathbf{x}_t) \propto q_{1|t}(\mathbf{x}_1 | \mathbf{x}_t) \exp(-J(\mathbf{x}_1))$. Assume $q_{1|t}(\mathbf{x}_1 | \mathbf{x}_t) = \mathcal{N}(\boldsymbol{\mu}, \boldsymbol{\Sigma}_t)$ and let $\mathbf{z}_t \triangleq \mathbf{x}_1 - \boldsymbol{\mu}$, so that $\mathbf{z}_t \sim q_t(\mathbf{z}_t) = \mathcal{N}(\mathbf{0}, \boldsymbol{\Sigma}_t)$. Let $\mathbf{B}_t \triangleq \nabla_{\mathbf{x}_t} \boldsymbol{\mu}(\mathbf{x}_t)$.

Since $q_{1|t}$ depends on \mathbf{x}_t only through $\boldsymbol{\mu}(\mathbf{x}_t)$, we have

$$\log q_{1|t}(\mathbf{x}_1 | \mathbf{x}_t) = -\frac{1}{2}(\mathbf{x}_1 - \boldsymbol{\mu})^\top \boldsymbol{\Sigma}_t^{-1}(\mathbf{x}_1 - \boldsymbol{\mu}) + \text{const},$$

and differentiating w.r.t. \mathbf{x}_t yields

$$\nabla_{\mathbf{x}_t} \log q_{1|t}(\mathbf{x}_1 | \mathbf{x}_t) = \mathbf{B}_t^\top \boldsymbol{\Sigma}_t^{-1}(\mathbf{x}_1 - \boldsymbol{\mu}) = \mathbf{B}_t^\top \boldsymbol{\Sigma}_t^{-1} \mathbf{z}_t. \quad (47)$$

For the true conditional, Bayes' rule gives $\log p_{1|t}(\mathbf{x}_1 | \mathbf{x}_t) = \log p_{t|1}(\mathbf{x}_t | \mathbf{x}_1) - \log p_t(\mathbf{x}_t)$. With $p_{t|1}(\mathbf{x}_t | \mathbf{x}_1) = \mathcal{N}(\alpha_t \mathbf{x}_1, \sigma_t^2 \mathbf{I})$,

$$\nabla_{\mathbf{x}_t} \log p_{t|1}(\mathbf{x}_t | \mathbf{x}_1) = \sigma_t^{-2}(\alpha_t \mathbf{x}_1 - \mathbf{x}_t),$$

and the Tweedie identity implies $\nabla_{\mathbf{x}_t} \log p_t(\mathbf{x}_t) = \sigma_t^{-2}(\alpha_t \boldsymbol{\mu} - \mathbf{x}_t)$. Therefore,

$$\nabla_{\mathbf{x}_t} \log p_{1|t}(\mathbf{x}_1 | \mathbf{x}_t) = \frac{\alpha_t}{\sigma_t^2} (\mathbf{x}_1 - \boldsymbol{\mu}) = \frac{\alpha_t}{\sigma_t^2} \mathbf{z}_t. \quad (48)$$

Subtracting the two guidance terms and using equation 47–equation 48 gives

$$\mathbf{g}_t^{\text{LGD}} - \mathbf{g}_t^{\text{SIM}} = \frac{b_t \sigma_t^2}{\alpha_t} \mathbb{E}_{q_{1|t}^{(J)}} \left[\left(\mathbf{B}_t^\top \boldsymbol{\Sigma}_t^{-1} - \frac{\alpha_t}{\sigma_t^2} \mathbf{I} \right) \mathbf{z}_t \right]. \quad (49)$$

Noting that $\mathbf{x}_1 = \boldsymbol{\mu} + \mathbf{z}_t$, the tilted law $q_{1|t}^{(J)}$ induces a tilted law on \mathbf{z}_t : $q_t^{(J_t)}(\mathbf{z}_t) \propto q_t(\mathbf{z}_t) \exp(-J_t(\mathbf{z}_t))$ with $J_t(\mathbf{z}_t) = J(\boldsymbol{\mu} + \mathbf{z}_t)$. Hence the expectation in equation 49 can be written under $q_t^{(J_t)}$.

Define the covariance mismatch

$$\boldsymbol{\Delta}_t(\mathbf{x}_t) \triangleq \boldsymbol{\Sigma}_t - \frac{\sigma_t^2}{\alpha_t} \mathbf{B}_t, \quad e_t(\mathbf{x}_t) \triangleq \|\boldsymbol{\Delta}_t(\mathbf{x}_t)\|_2^2.$$

Then $\mathbf{B}_t - \frac{\alpha_t}{\sigma_t^2} \boldsymbol{\Sigma}_t = -\frac{\alpha_t}{\sigma_t^2} \boldsymbol{\Delta}_t(\mathbf{x}_t)$, and since $\boldsymbol{\Sigma}_t$ is symmetric,

$$\mathbf{B}_t^\top \boldsymbol{\Sigma}_t^{-1} - \frac{\alpha_t}{\sigma_t^2} \mathbf{I} = (\boldsymbol{\Sigma}_t^{-1}(\mathbf{B}_t - \frac{\alpha_t}{\sigma_t^2} \boldsymbol{\Sigma}_t))^\top = -\frac{\alpha_t}{\sigma_t^2} (\boldsymbol{\Sigma}_t^{-1} \boldsymbol{\Delta}_t(\mathbf{x}_t))^\top.$$

Substituting into equation 49 yields

$$\mathbf{g}_t^{\text{LGD}} - \mathbf{g}_t^{\text{SIM}} = -b_t \mathbb{E}_{q_t^{(J_t)}} \left[(\boldsymbol{\Sigma}_t^{-1} \boldsymbol{\Delta}_t(\mathbf{x}_t))^\top \mathbf{z}_t \right]. \quad (50)$$

Finally, by Jensen's inequality,

$$\|\mathbf{g}_t^{\text{LGD}} - \mathbf{g}_t^{\text{SIM}}\|_2^2 \leq b_t^2 \mathbb{E}_{q_t^{(J_t)}} \left[\left\| (\boldsymbol{\Sigma}_t^{-1} \boldsymbol{\Delta}_t(\mathbf{x}_t))^\top \mathbf{z}_t \right\|_2^2 \right].$$

Using $\|A\mathbf{z}\|_2 \leq \|A\|_2 \|\mathbf{z}\|_2$ and submultiplicativity,

$$\left\| (\boldsymbol{\Sigma}_t^{-1} \boldsymbol{\Delta}_t(\mathbf{x}_t))^\top \mathbf{z}_t \right\|_2^2 \leq \|\boldsymbol{\Sigma}_t^{-1}\|_2^2 \|\boldsymbol{\Delta}_t(\mathbf{x}_t)\|_2^2 \|\mathbf{z}_t\|_2^2.$$

Taking expectation under $q_t^{(J_t)}$ and substituting $e_t(\mathbf{x}_t) = \|\boldsymbol{\Delta}_t(\mathbf{x}_t)\|_2^2$ gives

$$\|\mathbf{g}_t^{\text{LGD}} - \mathbf{g}_t^{\text{SIM}}\|_2^2 \leq b_t^2 \|\boldsymbol{\Sigma}_t^{-1}\|_2^2 \mathbb{E}_{q_t^{(J_t)}} [\|\mathbf{z}_t\|_2^2] e_t(\mathbf{x}_t),$$

which concludes the proof. \square

B.3. Proof of Theorem 2.3

Proof. Recall that

$$\nabla_{\mathbf{x}_t} \mathbb{E}_{p_{1|t}(\mathbf{x}_1|\mathbf{x}_t)}[\mathbf{x}_1] = -\frac{a_t}{b_t} \mathbf{I} + \frac{1}{b_t} \nabla_{\mathbf{x}_t} \mathbf{v}_t(\mathbf{x}_t). \quad (51)$$

At iteration k , let $\mathbf{J}_k \approx \nabla_{\mathbf{x}_k} \mathbf{v}_{t_k}(\mathbf{x}_k)$ and define

$$\mathbf{B}_k \triangleq -\frac{a_{t_k}}{b_{t_k}} \mathbf{I} + \frac{1}{b_{t_k}} \mathbf{J}_k, \quad \iff \quad \mathbf{J}_k = b_{t_k} \mathbf{B}_k + a_{t_k} \mathbf{I}. \quad (52)$$

We approximate the Jacobian \mathbf{J}_{k+1} using the secant condition induced by the observed pair $(\mathbf{x}_k, \mathbf{v}_k), (\mathbf{x}_{k+1}, \mathbf{v}_{k+1})$, namely

$$\mathbf{J}_{k+1} \mathbf{s}_k = \mathbf{r}_k, \quad \mathbf{s}_k = \mathbf{x}_{k+1} - \mathbf{x}_k, \quad \mathbf{r}_k = \mathbf{v}_{k+1} - \mathbf{v}_k. \quad (53)$$

Using equation 52 at time t_k , introduce the scaled matrix

$$\tilde{\mathbf{B}}_{k+1} \triangleq -\frac{a_{t_k}}{b_{t_k}} \mathbf{I} + \frac{1}{b_{t_k}} \mathbf{J}_{k+1}, \quad (54)$$

so that $\mathbf{J}_{k+1} = b_{t_k} \tilde{\mathbf{B}}_{k+1} + a_{t_k} \mathbf{I}$. Substituting this into equation 53 yields the equivalent secant equation

$$\tilde{\mathbf{B}}_{k+1} \mathbf{s}_k = -\frac{a_{t_k}}{b_{t_k}} \mathbf{s}_k + \frac{1}{b_{t_k}} \mathbf{r}_k \triangleq \mathbf{y}_k, \quad (55)$$

which matches the definition of \mathbf{y}_k in the theorem.

The secant constraint equation 55 does not identify a unique matrix. To obtain a stable and covariance-compatible estimate, we impose (i) symmetry, and (ii) a least-change principle:

$$\tilde{\mathbf{B}}_{k+1} = \arg \min_{\mathbf{B} = \mathbf{B}^\top} \|\mathbf{B} - \mathbf{B}_k\| \quad \text{s.t.} \quad \mathbf{B} \mathbf{s}_k = \mathbf{y}_k. \quad (56)$$

With the standard quasi-Newton choice of norm that yields a symmetric positive-definite update (the same setting used to derive the DFP/BFGS family; see (Nocedal & Wright, 2006)), the unique minimizer of equation 56 has the closed form

$$\tilde{\mathbf{B}}_{k+1} = \mathbf{V}_k^\top \mathbf{B}_k \mathbf{V}_k + \rho_k \mathbf{y}_k \mathbf{y}_k^\top, \quad \rho_k = \frac{1}{\mathbf{y}_k^\top \mathbf{s}_k}, \quad \mathbf{V}_k = \mathbf{I} - \rho_k \mathbf{s}_k \mathbf{y}_k^\top. \quad (57)$$

We briefly verify feasibility: symmetry is immediate from $\mathbf{B}_k = \mathbf{B}_k^\top$ and the rank-one term. Moreover, since $\mathbf{V}_k \mathbf{s}_k = \mathbf{s}_k - \rho_k \mathbf{s}_k (\mathbf{y}_k^\top \mathbf{s}_k) = \mathbf{0}$,

$$\tilde{\mathbf{B}}_{k+1} \mathbf{s}_k = \mathbf{V}_k^\top \mathbf{B}_k (\mathbf{V}_k \mathbf{s}_k) + \rho_k \mathbf{y}_k (\mathbf{y}_k^\top \mathbf{s}_k) = \mathbf{y}_k, \quad (58)$$

so equation 55 holds.

Finally, the matrix \mathbf{B}_{k+1} in the theorem is defined at time t_{k+1} :

$$\mathbf{B}_{k+1} = -\frac{a_{t_{k+1}}}{b_{t_{k+1}}} \mathbf{I} + \frac{1}{b_{t_{k+1}}} \mathbf{J}_{k+1}. \quad (59)$$

Combining equation 59 with equation 54 gives the affine relation

$$\mathbf{B}_{k+1} = \frac{b_{t_k}}{b_{t_{k+1}}} \tilde{\mathbf{B}}_{k+1} + \frac{a_{t_k} - a_{t_{k+1}}}{b_{t_{k+1}}} \mathbf{I} \triangleq u_k \tilde{\mathbf{B}}_{k+1} + w_k \mathbf{I}, \quad (60)$$

where $u_k = b_{t_k}/b_{t_{k+1}}$ and $w_k = (a_{t_k} - a_{t_{k+1}})/b_{t_{k+1}}$. Substituting equation 57 completes the claimed recursion:

$$\mathbf{B}_{k+1} = u_k (\mathbf{V}_k^\top \mathbf{B}_k \mathbf{V}_k + \rho_k \mathbf{y}_k \mathbf{y}_k^\top) + w_k \mathbf{I}. \quad (61)$$

□

B.4. Proof of Theorem 2.4

Proof. We prove by induction that the iterates produced by

$$\tilde{\mathbf{B}}_{k+1} = \mathbf{V}_k^\top \mathbf{B}_k \mathbf{V}_k + \rho_k \mathbf{y}_k \mathbf{y}_k^\top, \quad \mathbf{B}_{k+1} = u_k \tilde{\mathbf{B}}_{k+1} + w_k \mathbf{I}, \quad (62)$$

admit the claimed compact representation. Throughout, $\rho_k = (\mathbf{y}_k^\top \mathbf{s}_k)^{-1}$ and $\mathbf{V}_k = \mathbf{I} - \rho_k \mathbf{s}_k \mathbf{y}_k^\top$.

Base case. Initialize $\mathbf{B}_0 = \gamma_0 \mathbf{I}$, i.e., $\mathbf{U}_0 = []$ and $\mathbf{\Gamma}_0 = []$. For $k = 0$, using $\mathbf{V}_0 = \mathbf{I} - \rho_0 \mathbf{s}_0 \mathbf{y}_0^\top$ and expanding $\mathbf{V}_0^\top \mathbf{B}_0 \mathbf{V}_0 = \gamma_0 \mathbf{V}_0^\top \mathbf{V}_0$, we obtain

$$\begin{aligned} \tilde{\mathbf{B}}_1 &= \gamma_0 \mathbf{I} - \gamma_0 \rho_0 (\mathbf{y}_0 \mathbf{s}_0^\top + \mathbf{s}_0 \mathbf{y}_0^\top) + \gamma_0 \rho_0^2 (\mathbf{s}_0^\top \mathbf{s}_0) \mathbf{y}_0 \mathbf{y}_0^\top + \rho_0 \mathbf{y}_0 \mathbf{y}_0^\top \\ &= \gamma_0 \mathbf{I} + [\mathbf{s}_0 \quad \mathbf{y}_0] \begin{bmatrix} 0 & -\gamma_0 \rho_0 \\ -\gamma_0 \rho_0 & \rho_0 + \rho_0^2 \gamma_0 (\mathbf{s}_0^\top \mathbf{s}_0) \end{bmatrix} \begin{bmatrix} \mathbf{s}_0^\top \\ \mathbf{y}_0^\top \end{bmatrix}. \end{aligned} \quad (63)$$

Thus $\tilde{\mathbf{B}}_1 = \gamma_0 \mathbf{I} + \mathbf{U}_1 \tilde{\mathbf{\Gamma}}_1 \mathbf{U}_1^\top$ holds with $\mathbf{U}_1 = [\mathbf{s}_0, \mathbf{y}_0]$ and $\tilde{\mathbf{\Gamma}}_1$ given by the 2×2 matrix in equation 63. Applying equation 62 yields $\mathbf{B}_1 = (u_0 \gamma_0 + w_0) \mathbf{I} + \mathbf{U}_1 (u_0 \tilde{\mathbf{\Gamma}}_1) \mathbf{U}_1^\top$, so the claim holds for $k = 1$ with $\gamma_1 = u_0 \gamma_0 + w_0$ and $\mathbf{\Gamma}_1 = u_0 \tilde{\mathbf{\Gamma}}_1$. (If one uses a different column ordering for \mathbf{U}_1 , the corresponding $\mathbf{\Gamma}_1$ is obtained by the same permutation.)

Inductive step. Assume that for some $k \geq 1$,

$$\mathbf{B}_k = \gamma_k \mathbf{I} + \mathbf{U}_k \mathbf{\Gamma}_k \mathbf{U}_k^\top, \quad (64)$$

where $\mathbf{U}_k \in \mathbb{R}^{d \times m}$ collects past secant vectors and $\mathbf{\Gamma}_k \in \mathbb{R}^{m \times m}$. Define

$$\mathbf{p}_k \triangleq \mathbf{\Gamma}_k \mathbf{U}_k^\top \mathbf{s}_k, \quad \tau_k \triangleq \mathbf{s}_k^\top \mathbf{U}_k \mathbf{\Gamma}_k \mathbf{U}_k^\top \mathbf{s}_k, \quad \delta_k \triangleq \tau_k + \gamma_k \mathbf{s}_k^\top \mathbf{s}_k. \quad (65)$$

Then

$$\mathbf{B}_k \mathbf{s}_k = \gamma_k \mathbf{s}_k + \mathbf{U}_k \mathbf{p}_k, \quad \mathbf{s}_k^\top \mathbf{B}_k \mathbf{s}_k = \delta_k. \quad (66)$$

Using $\mathbf{V}_k = \mathbf{I} - \rho_k \mathbf{s}_k \mathbf{y}_k^\top$, we expand

$$\begin{aligned} \mathbf{V}_k^\top \mathbf{B}_k \mathbf{V}_k &= (\mathbf{I} - \rho_k \mathbf{s}_k \mathbf{y}_k^\top) \mathbf{B}_k (\mathbf{I} - \rho_k \mathbf{s}_k \mathbf{y}_k^\top) \\ &= \mathbf{B}_k - \rho_k \mathbf{B}_k \mathbf{s}_k \mathbf{y}_k^\top - \rho_k \mathbf{y}_k \mathbf{s}_k^\top \mathbf{B}_k + \rho_k^2 \mathbf{y}_k (\mathbf{s}_k^\top \mathbf{B}_k \mathbf{s}_k) \mathbf{y}_k^\top. \end{aligned} \quad (67)$$

Substituting equation 66 into equation 67 gives

$$\mathbf{V}_k^\top \mathbf{B}_k \mathbf{V}_k = \mathbf{B}_k - \rho_k (\gamma_k \mathbf{s}_k + \mathbf{U}_k \mathbf{p}_k) \mathbf{y}_k^\top - \rho_k \mathbf{y}_k (\gamma_k \mathbf{s}_k^\top + \mathbf{p}_k^\top \mathbf{U}_k^\top) + \rho_k^2 \delta_k \mathbf{y}_k \mathbf{y}_k^\top. \quad (68)$$

Adding the rank-one term $\rho_k \mathbf{y}_k \mathbf{y}_k^\top$ yields

$$\begin{aligned} \tilde{\mathbf{B}}_{k+1} &= \mathbf{V}_k^\top \mathbf{B}_k \mathbf{V}_k + \rho_k \mathbf{y}_k \mathbf{y}_k^\top \\ &= \mathbf{B}_k - \rho_k \mathbf{U}_k \mathbf{p}_k \mathbf{y}_k^\top - \rho_k \mathbf{y}_k \mathbf{p}_k^\top \mathbf{U}_k^\top - \gamma_k \rho_k (\mathbf{s}_k \mathbf{y}_k^\top + \mathbf{y}_k \mathbf{s}_k^\top) + \rho_k (1 + \rho_k \delta_k) \mathbf{y}_k \mathbf{y}_k^\top. \end{aligned} \quad (69)$$

Now substitute the induction hypothesis equation 64 into equation 69 and group terms. Let

$$\mathbf{U}_{k+1} \triangleq [\mathbf{U}_k \quad \mathbf{s}_k \quad \mathbf{y}_k]. \quad (70)$$

A direct multiplication shows that

$$\tilde{\mathbf{B}}_{k+1} = \gamma_k \mathbf{I} + \mathbf{U}_{k+1} \tilde{\mathbf{\Gamma}}_{k+1} \mathbf{U}_{k+1}^\top, \quad (71)$$

where

$$\tilde{\mathbf{\Gamma}}_{k+1} = \begin{bmatrix} \mathbf{\Gamma}_k & \mathbf{0} & -\rho_k \mathbf{p}_k \\ \mathbf{0}^\top & 0 & -\gamma_k \rho_k \\ -\rho_k \mathbf{p}_k^\top & -\gamma_k \rho_k & \rho_k (1 + \rho_k \delta_k) \end{bmatrix}, \quad \delta_k = \tau_k + \gamma_k \mathbf{s}_k^\top \mathbf{s}_k. \quad (72)$$

Indeed, the top-left block reproduces $\mathbf{U}_k \mathbf{\Gamma}_k \mathbf{U}_k^\top$, the off-diagonal blocks $-\rho_k \mathbf{p}_k$ reproduce the cross terms $-\rho_k \mathbf{U}_k \mathbf{p}_k \mathbf{y}_k^\top - \rho_k \mathbf{y}_k \mathbf{p}_k^\top \mathbf{U}_k^\top$, the entries $-\gamma_k \rho_k$ reproduce $-\gamma_k \rho_k (\mathbf{s}_k \mathbf{y}_k^\top + \mathbf{y}_k \mathbf{s}_k^\top)$, and the bottom-right entry gives the coefficient of $\mathbf{y}_k \mathbf{y}_k^\top$ in equation 69.

Finally, applying the affine update in equation 62 to equation 71 gives

$$\mathbf{B}_{k+1} = u_k \tilde{\mathbf{B}}_{k+1} + w_k \mathbf{I} = (u_k \gamma_k + w_k) \mathbf{I} + \mathbf{U}_{k+1} (u_k \tilde{\boldsymbol{\Gamma}}_{k+1}) \mathbf{U}_{k+1}^\top. \quad (73)$$

Therefore the representation holds at $k + 1$ with

$$\gamma_{k+1} = u_k \gamma_k + w_k, \quad \boldsymbol{\Gamma}_{k+1} = u_k \tilde{\boldsymbol{\Gamma}}_{k+1}, \quad (74)$$

and substituting equation 72 yields exactly the stated recursion. \square

B.5. Proof of Theorem 2.5

Proof. Let $\mathbf{B} = \gamma \mathbf{I} + \mathbf{U} \boldsymbol{\Gamma} \mathbf{U}^\top$ with $\gamma > 0$. Take the reduced QR factorization of $\mathbf{U} \in \mathbb{R}^{d \times m}$:

$$\mathbf{U} = \mathbf{Q} \mathbf{R}, \quad \mathbf{Q} \in \mathbb{R}^{d \times m}, \quad \mathbf{Q}^\top \mathbf{Q} = \mathbf{I}_m, \quad \mathbf{R} \in \mathbb{R}^{m \times m} \text{ upper triangular.} \quad (75)$$

Extend \mathbf{Q} to an orthonormal basis of \mathbb{R}^d by choosing $\mathbf{Q}_\perp \in \mathbb{R}^{d \times (d-m)}$ such that

$$\mathbf{P} \triangleq [\mathbf{Q}, \mathbf{Q}_\perp] \text{ is orthogonal,} \quad \mathbf{P}^\top \mathbf{P} = \mathbf{I}_d, \quad \mathbf{Q} \mathbf{Q}^\top + \mathbf{Q}_\perp \mathbf{Q}_\perp^\top = \mathbf{I}_d. \quad (76)$$

Using $\mathbf{U} = \mathbf{Q} \mathbf{R}$, we rewrite

$$\mathbf{B} = \gamma \mathbf{I} + \mathbf{Q} \mathbf{R} \boldsymbol{\Gamma} \mathbf{R}^\top \mathbf{Q}^\top. \quad (77)$$

Conjugating by the orthogonal matrix \mathbf{P} yields a block diagonal form:

$$\begin{aligned} \mathbf{P}^\top \mathbf{B} \mathbf{P} &= \begin{bmatrix} \mathbf{Q}^\top \\ \mathbf{Q}_\perp \end{bmatrix} (\gamma \mathbf{I} + \mathbf{Q} \mathbf{R} \boldsymbol{\Gamma} \mathbf{R}^\top \mathbf{Q}^\top) [\mathbf{Q} \quad \mathbf{Q}_\perp] \\ &= \begin{bmatrix} \gamma \mathbf{I}_m + \mathbf{R} \boldsymbol{\Gamma} \mathbf{R}^\top & \mathbf{0} \\ \mathbf{0} & \gamma \mathbf{I}_{d-m} \end{bmatrix}. \end{aligned} \quad (78)$$

Define the $m \times m$ matrix (consistent with Theorem 2.5)

$$\mathbf{C} \triangleq \gamma \mathbf{I}_m + \mathbf{R} \boldsymbol{\Gamma} \mathbf{R}^\top. \quad (79)$$

Assuming $\mathbf{B} \succ \mathbf{0}$, we have $\mathbf{P}^\top \mathbf{B} \mathbf{P} \succ \mathbf{0}$ since \mathbf{P} is orthogonal. By equation 78, this implies $\mathbf{C} \succ \mathbf{0}$, so \mathbf{C} admits a (lower) Cholesky factorization

$$\mathbf{C} = \mathbf{L}_C \mathbf{L}_C^\top. \quad (80)$$

We now construct \mathbf{L} such that $\mathbf{B} = \mathbf{L} \mathbf{L}^\top$. Consider the matrix

$$\tilde{\mathbf{L}} \triangleq \begin{bmatrix} \mathbf{L}_C & \mathbf{0} \\ \mathbf{0} & \sqrt{\gamma} \mathbf{I}_{d-m} \end{bmatrix} \in \mathbb{R}^{d \times d}. \quad (81)$$

Then by direct multiplication,

$$\tilde{\mathbf{L}} \tilde{\mathbf{L}}^\top = \begin{bmatrix} \mathbf{L}_C \mathbf{L}_C^\top & \mathbf{0} \\ \mathbf{0} & \gamma \mathbf{I}_{d-m} \end{bmatrix} = \begin{bmatrix} \mathbf{C} & \mathbf{0} \\ \mathbf{0} & \gamma \mathbf{I}_{d-m} \end{bmatrix}. \quad (82)$$

Combining with equation 78 and the fact that \mathbf{P} is orthogonal, we obtain

$$\mathbf{B} = \mathbf{P} \begin{bmatrix} \mathbf{C} & \mathbf{0} \\ \mathbf{0} & \gamma \mathbf{I}_{d-m} \end{bmatrix} \mathbf{P}^\top = (\mathbf{P} \tilde{\mathbf{L}} \mathbf{P}^\top) (\mathbf{P} \tilde{\mathbf{L}} \mathbf{P}^\top)^\top. \quad (83)$$

Therefore, one valid factor is

$$\mathbf{L}_* = \mathbf{P} \tilde{\mathbf{L}} \mathbf{P}^\top = \mathbf{Q} \mathbf{L}_C \mathbf{L}_C^\top + \sqrt{\gamma} \mathbf{Q}_\perp \mathbf{Q}_\perp^\top. \quad (84)$$

To eliminate the explicit dependence on \mathbf{Q}_\perp , we use the projector identity from equation 76:

$$\mathbf{Q}_\perp \mathbf{Q}_\perp^\top = \mathbf{I} - \mathbf{Q} \mathbf{Q}^\top. \quad (85)$$

Substituting into equation 84 gives

$$\mathbf{L}_* = \mathbf{Q} \mathbf{L}_C \mathbf{L}_C^\top + \sqrt{\gamma} (\mathbf{I} - \mathbf{Q} \mathbf{Q}^\top) = \mathbf{Q} (\mathbf{L}_C - \sqrt{\gamma} \mathbf{I}_m) \mathbf{Q}^\top + \sqrt{\gamma} \mathbf{I}. \quad (86)$$

Finally, since $\mathbf{B} = \mathbf{L}_* \mathbf{L}_*^\top$ by construction, taking $\mathbf{L} \equiv \mathbf{L}_*$ proves the claim. \square

C. Additional Analysis of Theorem

C.1. Relationship between $\mathcal{J}_{\text{SKL}}^{(\lambda)}$ and the MSE Loss

A common way to train a cost predictor under a control signal λ is to regress the energy values with an MSE objective,

$$\mathcal{J}_{\text{MSE}}^{(\lambda)}(\theta) = \mathbb{E}_{p(\mathbf{x})} \left[(J_\theta(\mathbf{x}, \lambda) - J(\mathbf{x}, \lambda))^2 \right], \quad \mathcal{L}_{\text{MSE}}^{(\lambda)}(\mathcal{B}, \theta) = \frac{1}{|\mathcal{B}|} \sum_{\mathbf{x} \in \mathcal{B}} (J_\theta(\mathbf{x}, \lambda) - J(\mathbf{x}, \lambda))^2. \quad (87)$$

While MSE is appropriate for approximating *energy values*, it does not directly align with the induced guided distribution $p^{(J, \lambda)}(\mathbf{x}) \propto p(\mathbf{x}) \exp(-J(\mathbf{x}, \lambda))$. This mismatch leads to two practical issues.

(1) Lack of shift invariance. Adding a λ -dependent constant to the energy does not change the induced distribution:

$$\tilde{J}(\mathbf{x}, \lambda) = J(\mathbf{x}, \lambda) + c(\lambda) \implies p^{(J, \lambda)}(\mathbf{x}) = p^{(\tilde{J}, \lambda)}(\mathbf{x}). \quad (88)$$

However, such a shift generally changes $\mathcal{J}_{\text{MSE}}^{(\lambda)}(\theta)$, imposing an unnecessary constraint that is irrelevant to distribution matching.

(2) Uniform weighting across λ scales. A standard parameterization treats λ as a scale that trades off quality and constraint strength,

$$J(\mathbf{x}, \lambda) = \lambda J(\mathbf{x}). \quad (89)$$

When λ is large, $p^{(J, \lambda)}$ concentrates near low-cost regions, so errors in J_θ near minima matter more than errors elsewhere. MSE, however, weights samples from p uniformly and does not adapt its emphasis with λ .

From MSE to SKL. As a distribution-matching alternative, Sec. 2.2 uses the symmetric KL divergence between the induced distributions $p^{(J, \lambda)}$ and $p^{(J_\theta, \lambda)}$, which can be written as

$$\mathcal{J}_{\text{SKL}}^{(\lambda)}(\theta) = \mathbb{E}_{p(\mathbf{x})} \left[(J_\theta(\mathbf{x}, \lambda) - J(\mathbf{x}, \lambda)) (w^{(J, \lambda)}(\mathbf{x}) - w^{(J_\theta, \lambda)}(\mathbf{x})) \right], \quad (90)$$

where

$$w^{(J, \lambda)}(\mathbf{x}) = \frac{\exp(-J(\mathbf{x}, \lambda))}{\mathbb{E}_{p(\mathbf{x})}[\exp(-J(\mathbf{x}, \lambda))]}, \quad w^{(J_\theta, \lambda)}(\mathbf{x}) = \frac{\exp(-J_\theta(\mathbf{x}, \lambda))}{\mathbb{E}_{p(\mathbf{x})}[\exp(-J_\theta(\mathbf{x}, \lambda))]}.$$

The normalized weights focus the loss on regions that dominate the guided distribution, and this emphasis becomes sharper as λ increases under equation 89.

Theorem C.1 (An upper bound and a counterexample). *Assume the scaled form equation 89 and the corresponding predictor scaling $J_\theta(\mathbf{x}, \lambda) = \lambda J_\theta(\mathbf{x})$. Define*

$$\mathcal{J}_{\text{EXP}}^{(\lambda)}(\theta) = \mathbb{E}_{p(\mathbf{x})} \left[(w^{(J_\theta, \lambda)}(\mathbf{x}) - w^{(J, \lambda)}(\mathbf{x}))^2 \right]. \quad (92)$$

Then

$$\mathcal{J}_{\text{SKL}}^{(\lambda)}(\theta) \leq \sqrt{\mathcal{J}_{\text{MSE}}^{(\lambda)}(\theta) \mathcal{J}_{\text{EXP}}^{(\lambda)}(\theta)}. \quad (93)$$

Moreover, there exists a sequence $\{\theta_i\}$ such that $\mathcal{J}_{\text{MSE}}^{(\lambda)}(\theta_i) \rightarrow 0$ while $\mathcal{J}_{\text{SKL}}^{(\lambda)}(\theta_i) \rightarrow \infty$.

Proof. For equation 93, apply Cauchy–Schwarz to equation 90:

$$|\mathcal{J}_{\text{SKL}}^{(\lambda)}(\theta)| \leq \sqrt{\mathbb{E}_p[(J_\theta(\mathbf{x}, \lambda) - J(\mathbf{x}, \lambda))^2]} \sqrt{\mathbb{E}_p[(w^{(J, \lambda)}(\mathbf{x}) - w^{(J_\theta, \lambda)}(\mathbf{x}))^2]}.$$

For the second claim, consider a one-dimensional setting with a continuous density $p(x)$ satisfying $0 < p(1) < \infty$. Let $J(x) = x^2$ and define a perturbed predictor

$$J_\varepsilon(x) = J(x) - \delta_\varepsilon b_\varepsilon(x),$$

where b_ε is a bump function supported on $A_\varepsilon = [1 - \varepsilon, 1 + \varepsilon]$, satisfies $0 \leq b_\varepsilon \leq 1$, and equals 1 on $B_\varepsilon = [1 - \varepsilon/2, 1 + \varepsilon/2]$ (hence $1_{B_\varepsilon} \leq b_\varepsilon \leq 1_{A_\varepsilon}$). Under equation 89, $J(\cdot, \lambda) = \lambda J(\cdot)$ and $J_\varepsilon(\cdot, \lambda) = \lambda J_\varepsilon(\cdot)$.

MSE. Since $J_\varepsilon - J = -\delta_\varepsilon b_\varepsilon$,

$$\mathcal{J}_{\text{MSE}}^{(\lambda)}(\varepsilon) = \mathbb{E}_p[(\lambda \delta_\varepsilon b_\varepsilon(x))^2] \leq \lambda^2 \delta_\varepsilon^2 \mathbb{P}_p(x \in A_\varepsilon) = O(\lambda^2 \delta_\varepsilon^2 \varepsilon).$$

SKL. Using equation 90 and $b_\varepsilon \geq 1_{B_\varepsilon}$,

$$\begin{aligned} \mathcal{J}_{\text{SKL}}^{(\lambda)}(\varepsilon) &= \mathbb{E}_p[(\lambda \delta_\varepsilon b_\varepsilon(x))(w^{(J_\varepsilon, \lambda)}(x) - w^{(J, \lambda)}(x))] = \lambda \delta_\varepsilon \left(\mathbb{E}_{p^{(J_\varepsilon, \lambda)}}[b_\varepsilon] - \mathbb{E}_{p^{(J, \lambda)}}[b_\varepsilon] \right) \\ &\geq \lambda \delta_\varepsilon \mathbb{P}_{p^{(J_\varepsilon, \lambda)}}(x \in B_\varepsilon) - \lambda \delta_\varepsilon \mathbb{P}_{p^{(J, \lambda)}}(x \in A_\varepsilon). \end{aligned}$$

The second term is $O(\lambda \delta_\varepsilon \varepsilon)$. For the first term,

$$\mathbb{P}_{p^{(J_\varepsilon, \lambda)}}(x \in B_\varepsilon) = \frac{\int_{B_\varepsilon} e^{-\lambda J_\varepsilon(x)} p(x) dx}{\int_{\mathbb{R}} e^{-\lambda J_\varepsilon(x)} p(x) dx}.$$

Let $I(A) = \int_A e^{-\lambda J(x)} p(x) dx$. Since $J_\varepsilon(x) \leq J(x)$ on A_ε ,

$$\int_{B_\varepsilon} e^{-\lambda J_\varepsilon(x)} p(x) dx \geq e^{\lambda \delta_\varepsilon} I(B_\varepsilon), \quad \int_{\mathbb{R}} e^{-\lambda J_\varepsilon(x)} p(x) dx \leq I(\mathbb{R}) + (e^{\lambda \delta_\varepsilon} - 1) I(A_\varepsilon).$$

Choose δ_ε so that $e^{\lambda \delta_\varepsilon} I(B_\varepsilon) = I(\mathbb{R})/\varepsilon$, which gives $\delta_\varepsilon = \Theta(\lambda^{-1} \log(1/\varepsilon))$. Under mild regularity (boundedness of $e^{-\lambda J(x)}$ on A_ε), the ratio $I(A_\varepsilon)/I(B_\varepsilon)$ stays bounded as $\varepsilon \rightarrow 0$, and thus $\mathbb{P}_{p^{(J_\varepsilon, \lambda)}}(x \in B_\varepsilon)$ is bounded away from 0. Therefore $\mathcal{J}_{\text{SKL}}^{(\lambda)}(\varepsilon) = \Omega(\lambda \delta_\varepsilon) = \Omega(\log(1/\varepsilon)) \rightarrow \infty$, while $\mathcal{J}_{\text{MSE}}^{(\lambda)}(\varepsilon) = O(\lambda^2 \delta_\varepsilon^2 \varepsilon) = O(\varepsilon \log^2(1/\varepsilon)) \rightarrow 0$. \square

Theorem C.1 shows that minimizing MSE does not necessarily control the distributional error measured by SKL. The extra factor $\mathcal{J}_{\text{EXP}}^{(\lambda)}$ reflects how well the *normalized exponentials* match, which is closely related to matching the softmax weights on minibatches (Eq. 8).

Theorem C.2 (Small- and large- λ behavior). *Assume equation 89 and $J_\theta(\mathbf{x}, \lambda) = \lambda J_\theta(\mathbf{x})$.*

(i) As $\lambda \rightarrow 0$. If J and J_θ have finite second moments under p , then

$$\mathcal{J}_{\text{SKL}}^{(\lambda)}(\theta) = \lambda^2 \mathbb{V}_{p(\mathbf{x})}[J_\theta(\mathbf{x}) - J(\mathbf{x})] + o(\lambda^2) \leq \mathcal{J}_{\text{MSE}}^{(\lambda)}(\theta) + o(\lambda^2). \quad (94)$$

(ii) As $\lambda \rightarrow \infty$. Suppose J has a unique global minimizer $\mathbf{x}^ = \arg \min_{\mathbf{x}} J(\mathbf{x})$ and J_θ has a unique global minimizer $\mathbf{x}_\theta^* = \arg \min_{\mathbf{x}} J_\theta(\mathbf{x})$. Under standard regularity conditions for Laplace asymptotics,*

$$\mathcal{J}_{\text{SKL}}^{(\lambda)}(\theta) = \lambda \left(J_\theta(\mathbf{x}^*) - J_\theta(\mathbf{x}_\theta^*) + J(\mathbf{x}_\theta^*) - J(\mathbf{x}^*) \right) + o(1). \quad (95)$$

Proof. (i) Expand $w^{(J, \lambda)}$ for small λ :

$$e^{-\lambda J(\mathbf{x})} = 1 - \lambda J(\mathbf{x}) + O(\lambda^2), \quad \mathbb{E}_p[e^{-\lambda J(\mathbf{x})}] = 1 - \lambda \mathbb{E}_p[J(\mathbf{x})] + O(\lambda^2),$$

which yields

$$w^{(J, \lambda)}(\mathbf{x}) = 1 - \lambda(J(\mathbf{x}) - \mathbb{E}_p[J(\mathbf{x})]) + O(\lambda^2).$$

Applying the same expansion to $w^{(J_\theta, \lambda)}$ and substituting into equation 90 gives $\mathcal{J}_{\text{SKL}}^{(\lambda)}(\theta) = \lambda^2 \mathbb{V}_{p(\mathbf{x})}[J_\theta - J] + o(\lambda^2)$. The inequality follows from $\mathbb{V}_p(J_\theta - J) \leq \mathbb{E}_p[(J_\theta - J)^2]$ and $\mathcal{J}_{\text{MSE}}^{(\lambda)}(\theta) = \lambda^2 \mathbb{E}_p[(J_\theta - J)^2]$.

(ii) Using equation 90 and $\Delta(\mathbf{x}) = J_\theta(\mathbf{x}) - J(\mathbf{x})$,

$$\mathcal{J}_{\text{SKL}}^{(\lambda)}(\theta) = \lambda \left(\mathbb{E}_{p^{(J, \lambda)}}[\Delta(\mathbf{x})] - \mathbb{E}_{p^{(J_\theta, \lambda)}}[\Delta(\mathbf{x})] \right).$$

As $\lambda \rightarrow \infty$, $p^{(J, \lambda)}$ concentrates at \mathbf{x}^* and $p^{(J_\theta, \lambda)}$ concentrates at \mathbf{x}_θ^* , so Laplace asymptotics give $\mathbb{E}_{p^{(J, \lambda)}}[\Delta(\mathbf{x})] = \Delta(\mathbf{x}^*) + o(1)$ and $\mathbb{E}_{p^{(J_\theta, \lambda)}}[\Delta(\mathbf{x})] = \Delta(\mathbf{x}_\theta^*) + o(1)$, which yields equation 95. \square

Theorem C.2 highlights two regimes. For small λ , SKL behaves like a (scaled) variance of the prediction error and is therefore controlled by MSE. For large λ , SKL depends primarily on how well J_θ matches the *relative ordering* of low-cost regions, consistent with the fact that minibatch weights in Eq. 8 reduce to a low-temperature softmax that emphasizes near-minimum samples.

C.2. The choice of φ_k and the rationale for preserving positive definiteness

Our covariance construction relies on the factorization in Theorem 2.5, which requires $\mathbf{B}_k \succ 0$ and $\gamma_k > 0$. This condition is not merely technical. In our method, \mathbf{B}_k serves as a local proxy for the Jacobian-induced matrix that determines the Gaussian covariance; if \mathbf{B}_k loses positive definiteness, then (i) the implied covariance may become indefinite, and (ii) the matrix square-root used in sampling becomes ill-conditioned or undefined, which can destabilize the entire guidance procedure. We therefore enforce $\mathbf{B}_k \succ 0$ throughout sampling.

The update in Theorem 2.3 inherits the structure of quasi-Newton secant updates. As in DFP/BFGS-type methods, positive definiteness can be preserved if the curvature condition holds:

$$\mathbf{s}_k^\top \mathbf{y}_k > 0. \quad (96)$$

In classical optimization, one can enforce equation 96 by choosing step sizes that satisfy Wolfe conditions (Nocedal & Wright, 2006). In our setting, however, $\mathbf{s}_k = \mathbf{x}_{k+1} - \mathbf{x}_k$ is produced by a fixed-time ODE integrator along a prescribed time grid, and the “step size” cannot be freely adjusted. Consequently, equation 96 may fail, especially when the velocity field varies rapidly over time or when numerical error accumulates.

To guarantee equation 96 and maintain $\mathbf{B}_k \succ 0$, we use a damped secant vector and replace \mathbf{y}_k by

$$\hat{\mathbf{y}}_k = \varphi_k \mathbf{y}_k + (1 - \varphi_k) \mathbf{B}_k \mathbf{s}_k, \quad \varphi_k \in [0, 1]. \quad (97)$$

This interpolation has two effects. First, it enforces a controlled curvature:

$$\mathbf{s}_k^\top \hat{\mathbf{y}}_k = \varphi_k \mathbf{s}_k^\top \mathbf{y}_k + (1 - \varphi_k) \mathbf{s}_k^\top \mathbf{B}_k \mathbf{s}_k. \quad (98)$$

Since $\mathbf{B}_k \succ 0$ implies $\mathbf{s}_k^\top \mathbf{B}_k \mathbf{s}_k > 0$ for any nonzero \mathbf{s}_k , choosing φ_k sufficiently small guarantees $\mathbf{s}_k^\top \hat{\mathbf{y}}_k > 0$ even when $\mathbf{s}_k^\top \mathbf{y}_k \leq 0$. Second, it prevents overly aggressive updates: when $\varphi_k \rightarrow 0$, we have $\hat{\mathbf{y}}_k = \mathbf{B}_k \mathbf{s}_k$, and the secant update becomes an identity update. Indeed, with $\hat{\mathbf{y}}_k = \mathbf{B}_k \mathbf{s}_k$,

$$\mathbf{V}_k = \mathbf{I} - \rho_k \mathbf{s}_k \hat{\mathbf{y}}_k^\top = \mathbf{I} - \rho_k \mathbf{s}_k \mathbf{s}_k^\top \mathbf{B}_k, \quad \rho_k = \frac{1}{\hat{\mathbf{y}}_k^\top \mathbf{s}_k} = \frac{1}{\mathbf{s}_k^\top \mathbf{B}_k \mathbf{s}_k}, \quad (99)$$

and the standard symmetric secant update yields $\tilde{\mathbf{B}}_{k+1} = \mathbf{B}_k$, so the DFP/BFGS correction is effectively skipped and only the affine time-rescaling remains:

$$\mathbf{B}_{k+1} = u_k \mathbf{B}_k + w_k \mathbf{I}. \quad (100)$$

Thus, damping provides a continuous mechanism that interpolates between a full secant correction ($\varphi_k = 1$) and a conservative no-correction step ($\varphi_k = 0$).

We follow the standard damped-update design used in quasi-Newton methods (Powell, 1978; Byrd et al., 1994) and choose φ_k to keep the effective curvature within a controlled band relative to $\mathbf{s}_k^\top \mathbf{B}_k \mathbf{s}_k$. Define

$$\tau_k \triangleq \frac{\mathbf{s}_k^\top \mathbf{y}_k}{\mathbf{s}_k^\top \mathbf{B}_k \mathbf{s}_k}. \quad (101)$$

We then set

$$\varphi_k = \begin{cases} \frac{\sigma_2}{1 - \tau_k}, & \tau_k < 1 - \sigma_2, \\ \frac{\sigma_3}{\tau_k - 1}, & \tau_k > 1 + \sigma_3, \\ 1, & \text{otherwise,} \end{cases} \quad \sigma_2, \sigma_3 \in (0, 1). \quad (102)$$

This choice enforces

$$(1 - \sigma_2) \mathbf{s}_k^\top \mathbf{B}_k \mathbf{s}_k \leq \mathbf{s}_k^\top \hat{\mathbf{y}}_k \leq (1 + \sigma_3) \mathbf{s}_k^\top \mathbf{B}_k \mathbf{s}_k, \quad (103)$$

which follows by substituting equation 97 into equation 98 and using equation 101. In particular, the left inequality in equation 103 guarantees $\mathbf{s}_k^\top \hat{\mathbf{y}}_k > 0$ whenever $\mathbf{s}_k \neq 0$, so the curvature condition holds for the damped pair $(\mathbf{s}_k, \hat{\mathbf{y}}_k)$ even when the raw pair violates equation 96. As a result, the symmetric secant update in Theorem 2.3 preserves $\mathbf{B}_k \succ 0$ in the same sense as standard quasi-Newton updates.

D. Algorithms and time-complexity analysis.

D.1. Time-annealed optimization

Algorithm 2 Time-annealed optimization

```

1: Input: initial latent  $\mathbf{x}_0$ ; cost  $J(\mathbf{x}, \lambda)$ ; guidance scale  $\lambda > 0$ ; step size  $\eta$ ; iterations  $K$ ; velocity field  $\mathbf{v}_t(\mathbf{x})$ ; noise
   schedule  $(\alpha_t, \sigma_t)$ ; time bounds  $(t_{\min}, t_{\max})$ ; annealing lower bound  $t_{\min}^{(k)}$ .
2: Output: optimized latent  $\mathbf{x}_K$ .
3: for  $k = 0$  to  $K - 1$  do
4:   Sample  $t_k \sim \mathcal{U}(t_{\min}^{(k)}, t_{\max})$ 
5:    $\mathbf{x}_{t_k} \leftarrow \text{ADDNOISE}(\mathbf{x}_k, t_k)$ 
6:    $\mathbf{g} \leftarrow \nabla_{\mathbf{x}} J(\mathbf{x}_k, \lambda) - (\mathbf{v}_{t_k}(\mathbf{x}_{t_k}^k) - (\dot{\alpha}_{t_k}/\alpha_{t_k})\mathbf{x}_{t_k}^k)/s_{t_k}$ 
7:    $\mathbf{x}_{k+1} \leftarrow \mathbf{x}_k - \eta \mathbf{g}$ 
8: end for
9: return  $\mathbf{x}_K$ 

```

Time-annealed optimization. Alg. 2 performs gradient descent in the Shape-VAE latent space while explicitly counteracting distributional drift. At iteration k , we sample a noise level t_k from an annealed interval $[t_{\min}^{(k)}, t_{\max}]$ and perturb the current iterate via $\mathbf{x}_{t_k} \leftarrow \text{ADDNOISE}(\mathbf{x}_k, t_k)$ using the same schedule as the generative model. We then form an update direction $\mathbf{g} = \nabla_{\mathbf{x}} J(\mathbf{x}_k, \lambda) - (\mathbf{v}_{t_k}(\mathbf{x}_{t_k}^k) - (\dot{\alpha}_{t_k}/\alpha_{t_k})\mathbf{x}_{t_k}^k)/s_{t_k}$, where the first term improves the objective and the second term acts as a prior correction induced by the flow field, encouraging \mathbf{x}_k to remain in a plausible region of the learned shape distribution. Finally, we update $\mathbf{x}_{k+1} \leftarrow \mathbf{x}_k - \eta \mathbf{g}$ and repeat for K iterations.

Time complexity. Let d be the latent dimension. Denote by $C_{\text{DiT}}^{\text{fwd}}$ the cost of one forward evaluation of the velocity field $\mathbf{v}_t(\cdot)$, and by C_J^{bwd} the cost of computing $\nabla_{\mathbf{x}} J(\mathbf{x}, \lambda)$ via automatic differentiation (including forward and backward passes of the cost predictor). Each iteration requires: (i) one ADDNOISE and several vector operations, costing $\mathcal{O}(d)$; (ii) one DiT forward, costing $\mathcal{O}(C_{\text{DiT}}^{\text{fwd}})$; (iii) one cost-gradient evaluation, costing $\mathcal{O}(C_J^{\text{bwd}})$. Therefore, the total complexity over K iterations is

$$\mathcal{O}\left(K \left[C_{\text{DiT}}^{\text{fwd}} + C_J^{\text{bwd}} + d \right]\right).$$

The memory overhead (excluding model parameters) is $\mathcal{O}(d)$ for storing the current iterate and intermediate activations; in practice it is dominated by the activation memory of the cost predictor during backpropagation.

D.2. Damping (Damp.) algorithm

Algorithm 3 DAMP.($\mathbf{y}, \mathbf{s}, \gamma, \mathbf{U}, \mathbf{\Gamma}$)

```

1: Input: secant vectors  $\mathbf{s}, \mathbf{y}$ ; compact form  $(\gamma, \mathbf{U}, \mathbf{\Gamma})$  defining  $\mathbf{B} = \gamma \mathbf{I} + \mathbf{U} \mathbf{\Gamma} \mathbf{U}^{\top}$ ; parameters  $\sigma_2 \in (0, 1)$ ,  $\sigma_3 > 0$ .
2: Output: damped vector  $\hat{\mathbf{y}}$  and coefficient  $\varphi$ .
3:  $\mathbf{Bs} \leftarrow \text{APPLYB}(\mathbf{s}; \gamma, \mathbf{U}, \mathbf{\Gamma}) \{= \gamma \mathbf{s} + \mathbf{U} \mathbf{\Gamma} (\mathbf{U}^{\top} \mathbf{s})\}$ 
4:  $s^{\top} y \leftarrow \mathbf{s}^{\top} \mathbf{y}$ ,  $s^{\top} Bs \leftarrow \mathbf{s}^{\top} (\mathbf{Bs})$ .
5:  $\tau \leftarrow (s^{\top} y) / (s^{\top} Bs)$ .
6:  $\varphi \leftarrow 1$ .
7: if  $\tau < 1 - \sigma_2$  then
8:    $\varphi \leftarrow \sigma_2 / (1 - \tau)$ .
9: else if  $\tau > 1 + \sigma_3$  then
10:    $\varphi \leftarrow \sigma_3 / (\tau - 1)$ .
11: end if
12:  $\hat{\mathbf{y}} \leftarrow \varphi \mathbf{y} + (1 - \varphi) \mathbf{Bs}$ .
13: return  $(\hat{\mathbf{y}}, \varphi)$ .

```

Damping for positive definiteness. Alg. 3 enforces a curvature condition for the DFP-style secant update used in our covariance estimator. Given $\mathbf{B} = \gamma \mathbf{I} + \mathbf{U} \mathbf{\Gamma} \mathbf{U}^{\top}$ and a new secant pair (\mathbf{s}, \mathbf{y}) , we form the ratio $\tau = (s^{\top} y) / (s^{\top} Bs)$ and replace \mathbf{y} by a convex combination $\hat{\mathbf{y}} = \varphi \mathbf{y} + (1 - \varphi) \mathbf{Bs}$. The piecewise choice of φ guarantees $(1 - \sigma_2) s^{\top} \mathbf{Bs} \leq s^{\top} \hat{\mathbf{y}} \leq$

$(1 + \sigma_3) \mathbf{s}^\top \mathbf{B} \mathbf{s}$, so in particular $\mathbf{s}^\top \hat{\mathbf{y}} > 0$ whenever $\mathbf{B} \succ 0$. This preserves the positive definiteness of the updated \mathbf{B} and stabilizes the downstream matrix square-root used for Monte Carlo sampling.

Time complexity. Let d be the latent dimension and let r denote the rank of the compact representation (in our memory-queue implementation, $r = 2m$). The dominant computation in Alg. 3 is applying the compact secant operator to a vector,

$$\mathbf{B}\mathbf{s} = \gamma \mathbf{s} + \mathbf{U}\boldsymbol{\Gamma}(\mathbf{U}^\top \mathbf{s}).$$

Computing $\mathbf{U}^\top \mathbf{s}$ costs $\mathcal{O}(dr)$, multiplying by $\boldsymbol{\Gamma} \in \mathbb{R}^{r \times r}$ costs $\mathcal{O}(r^2)$, and multiplying by \mathbf{U} costs $\mathcal{O}(dr)$. All remaining operations (inner products, scalar branches, and the convex combination) are $\mathcal{O}(d)$. Therefore Alg. 3 runs in

$$\mathcal{O}(dr + r^2)$$

time per call. Storing the compact factors $(\mathbf{U}, \boldsymbol{\Gamma})$ requires $\mathcal{O}(dr + r^2)$ memory, and the algorithm uses an additional $\mathcal{O}(d)$ workspace.

D.3. UpdataB algorithm

Algorithm 4 UPDATEB($\mathcal{M}, \hat{\gamma}$)

```

1: Input: memory queue  $\mathcal{M} = \{(\mathbf{s}_i, \hat{\mathbf{y}}_i, u_i, w_i)\}_{i=0}^{\ell-1}$  (ordered from oldest to newest,  $\ell \leq m$ ); Jacobi-scale init  $\hat{\gamma} > 0$ .
2: Output: compact form  $(\gamma, \mathbf{U}, \boldsymbol{\Gamma})$  such that  $\mathbf{B} = \gamma \mathbf{I} + \mathbf{U}\boldsymbol{\Gamma}\mathbf{U}^\top$ .
3:  $\gamma \leftarrow \hat{\gamma}$ ,  $\mathbf{U} \leftarrow []$ ,  $\boldsymbol{\Gamma} \leftarrow []$ .
4: for  $i = 0$  to  $\ell - 1$  do
5:    $\mathbf{s} \leftarrow \mathbf{s}_i$ ,  $\hat{\mathbf{y}} \leftarrow \hat{\mathbf{y}}_i$ ,  $u \leftarrow u_i$ ,  $w \leftarrow w_i$ .
6:    $\rho \leftarrow 1/(\hat{\mathbf{y}}^\top \mathbf{s})$ .
7:   if  $\mathbf{U} = []$  then
8:      $\mathbf{U} \leftarrow [\mathbf{s}, \hat{\mathbf{y}}]$  {append columns}
9:      $\boldsymbol{\Gamma} \leftarrow \begin{bmatrix} 0 & -\gamma\rho \\ -\gamma\rho & \rho + \rho^2 \gamma \mathbf{s}^\top \mathbf{s} \end{bmatrix}$ .
10:  else
11:     $\mathbf{q} \leftarrow \mathbf{U}^\top \mathbf{s}$ .
12:     $\mathbf{p} \leftarrow \boldsymbol{\Gamma} \mathbf{q}$ ,  $\tau \leftarrow \mathbf{q}^\top \mathbf{p}$ .
13:     $\mathbf{U} \leftarrow [\mathbf{U}, \mathbf{s}, \hat{\mathbf{y}}]$ .
14:     $\boldsymbol{\Gamma} \leftarrow \begin{bmatrix} \boldsymbol{\Gamma} & \mathbf{0} & -\rho \mathbf{p} \\ \mathbf{0}^\top & 0 & -\gamma\rho \\ -\rho \mathbf{p}^\top & -\gamma\rho & \rho + \rho^2(\tau + \gamma \mathbf{s}^\top \mathbf{s}) \end{bmatrix}$ .
15:  end if
16:   $\boldsymbol{\Gamma} \leftarrow u \boldsymbol{\Gamma}$ ,  $\gamma \leftarrow u \gamma + w$ .
17: end for
18: return  $(\gamma, \mathbf{U}, \boldsymbol{\Gamma})$ .

```

Low-rank reconstruction of the secant matrix. Alg. 4 rebuilds the compact representation of the local Jacobian-induced matrix \mathbf{B} from the memory queue \mathcal{M} . Starting from a Jacobi-scale initialization $\gamma \leftarrow \hat{\gamma}$, it sequentially applies the DFP-form secant updates using the stored pairs $(\mathbf{s}_i, \hat{\mathbf{y}}_i)$, while accounting for the time-dependent affine transform $\mathbf{B} \leftarrow u_i \mathbf{B} + w_i \mathbf{I}$ induced by the schedule. At each iteration, the algorithm maintains \mathbf{B} in the form $\mathbf{B} = \gamma \mathbf{I} + \mathbf{U}\boldsymbol{\Gamma}\mathbf{U}^\top$, where \mathbf{U} stores the history of secant vectors (interleaving \mathbf{s} and $\hat{\mathbf{y}}$) and $\boldsymbol{\Gamma}$ stores the corresponding small dense coefficients. The scalars $\rho = (\hat{\mathbf{y}}^\top \mathbf{s})^{-1}$ and $\tau = \mathbf{q}^\top \mathbf{p}$ with $\mathbf{q} = \mathbf{U}^\top \mathbf{s}$, $\mathbf{p} = \boldsymbol{\Gamma} \mathbf{q}$ implement the closed-form recursion in Theorem 2.4, enabling updates without forming any $d \times d$ matrices.

Time complexity. Let d be the latent dimension and let $\ell \leq m$ denote the number of stored secant pairs. At iteration i , the compact rank is $r_i = 2i$. The dominant costs are forming $\mathbf{q} = \mathbf{U}^\top \mathbf{s}$ in $\mathcal{O}(dr_i)$, computing $\mathbf{p} = \boldsymbol{\Gamma} \mathbf{q}$ in $\mathcal{O}(r_i^2)$, and evaluating $\tau = \mathbf{q}^\top \mathbf{p}$ in $\mathcal{O}(r_i)$. All remaining operations (updating γ , assembling the new blocks, and scaling by u) are lower order. Summing over $i = 0, \dots, \ell - 1$ yields

$$\sum_{i=0}^{\ell-1} \mathcal{O}(dr_i + r_i^2) = \mathcal{O}\left(d \sum_{i=0}^{\ell-1} 2i + \sum_{i=0}^{\ell-1} (2i)^2\right) = \mathcal{O}(d\ell^2 + \ell^3).$$

Since $\ell \leq m$ and $r = 2m$, this can be equivalently expressed as $\mathcal{O}(dm^2 + m^3)$ in the worst case. The memory footprint is dominated by storing $\mathbf{U} \in \mathbb{R}^{d \times 2\ell}$ and $\mathbf{\Gamma} \in \mathbb{R}^{2\ell \times 2\ell}$, i.e., $\mathcal{O}(d\ell + \ell^2)$.

D.4. SemiNumericalSqrt algorithm

Algorithm 5 SEMINUMERICALSQRT($\gamma, \mathbf{U}, \mathbf{\Gamma}$)

- 1: **Input:** $\gamma > 0$, $\mathbf{U} \in \mathbb{R}^{d \times r}$, $\mathbf{\Gamma} \in \mathbb{R}^{r \times r}$ (symmetric).
- 2: **Output:** a linear map \mathbf{L} such that $\mathbf{B} = \gamma\mathbf{I} + \mathbf{U}\mathbf{\Gamma}\mathbf{U}^\top = \mathbf{L}\mathbf{L}^\top$.
- 3: **if** $r = 0$ **then**
- 4: **return** $\mathbf{L} = \sqrt{\gamma}\mathbf{I}$.
- 5: **end if**
- 6: Compute reduced QR: $\mathbf{U} = \mathbf{Q}\mathbf{R}$ with $\mathbf{Q} \in \mathbb{R}^{d \times r}$ orthonormal, $\mathbf{R} \in \mathbb{R}^{r \times r}$ upper-triangular.
- 7: Form the small matrix $\mathbf{C} \leftarrow \gamma\mathbf{I}_r + \mathbf{R}\mathbf{\Gamma}\mathbf{R}^\top$.
- 8: (stabilize) $\mathbf{C} \leftarrow (\mathbf{C} + \mathbf{C}^\top)/2$ and optionally $\mathbf{C} \leftarrow \mathbf{C} + \epsilon\mathbf{I}_r$.
- 9: Cholesky: $\mathbf{C} = \mathbf{L}_C\mathbf{L}_C^\top$ (lower-triangular \mathbf{L}_C).
- 10: Define \mathbf{L} implicitly by

$$\mathbf{L} = \sqrt{\gamma}\mathbf{I} + \mathbf{Q}(\mathbf{L}_C - \sqrt{\gamma}\mathbf{I}_r)\mathbf{Q}^\top.$$

- 11: **return** \mathbf{L} (implemented via $\text{APPLYL}(\mathbf{x}) = \sqrt{\gamma}\mathbf{x} + \mathbf{Q}(\mathbf{L}_C - \sqrt{\gamma}\mathbf{I})(\mathbf{Q}^\top\mathbf{x})$).
-

Semi-numerical square root in compact form. Alg. 5 computes a numerically stable factorization of the low-rank matrix $\mathbf{B} = \gamma\mathbf{I} + \mathbf{U}\mathbf{\Gamma}\mathbf{U}^\top$ without forming any $d \times d$ dense matrices. The key idea is to isolate the nontrivial action of \mathbf{B} to the r -dimensional subspace spanned by the columns of \mathbf{U} . Using the reduced QR factorization $\mathbf{U} = \mathbf{Q}\mathbf{R}$, we obtain

$$\mathbf{B} = \gamma\mathbf{I} + \mathbf{Q}(\mathbf{R}\mathbf{\Gamma}\mathbf{R}^\top)\mathbf{Q}^\top,$$

so the factorization reduces to taking a Cholesky decomposition of the small matrix $\mathbf{C} = \gamma\mathbf{I}_r + \mathbf{R}\mathbf{\Gamma}\mathbf{R}^\top$. The resulting square-root map is represented as a rank- r correction to $\sqrt{\gamma}\mathbf{I}$:

$$\mathbf{L} = \sqrt{\gamma}\mathbf{I} + \mathbf{Q}(\mathbf{L}_C - \sqrt{\gamma}\mathbf{I}_r)\mathbf{Q}^\top, \quad \mathbf{C} = \mathbf{L}_C\mathbf{L}_C^\top,$$

which can be applied to vectors using only matrix–vector products with \mathbf{Q} and \mathbf{L}_C . The symmetrization and optional diagonal jitter $\epsilon\mathbf{I}_r$ ensure numerical stability when \mathbf{C} is close to singular due to finite-precision errors.

Time complexity. Let d be the latent dimension and let r denote the compact rank (in our memory-queue implementation, $r = 2\ell \leq 2m$). Computing the reduced QR factorization of $\mathbf{U} \in \mathbb{R}^{d \times r}$ costs $\mathcal{O}(dr^2)$. Forming $\mathbf{C} = \gamma\mathbf{I}_r + \mathbf{R}\mathbf{\Gamma}\mathbf{R}^\top$ costs $\mathcal{O}(r^3)$ (e.g., one $r \times r$ multiply to form $\mathbf{R}\mathbf{\Gamma}$ and one to post-multiply by \mathbf{R}^\top), and the Cholesky factorization of $\mathbf{C} \in \mathbb{R}^{r \times r}$ also costs $\mathcal{O}(r^3)$. Therefore, the total preprocessing cost is

$$\mathcal{O}(dr^2 + r^3).$$

In practice, \mathbf{L} is never materialized as a dense $d \times d$ matrix. To apply \mathbf{L} to a vector $\mathbf{x} \in \mathbb{R}^d$, we compute $\mathbf{q} = \mathbf{Q}^\top\mathbf{x}$, $\mathbf{u} = (\mathbf{L}_C - \sqrt{\gamma}\mathbf{I}_r)\mathbf{q}$, and then \mathbf{Qu} , which costs $\mathcal{O}(dr + r^2)$ per application. The memory footprint is $\mathcal{O}(dr + r^2)$ to store \mathbf{Q} and the small factors (e.g., \mathbf{R} , $\mathbf{\Gamma}$, \mathbf{C} , and \mathbf{L}_C).

D.5. SampleTiltedMean algorithm

Tilted-mean estimator. Alg. 6 approximates the *tilted mean correction* that appears in our guidance term. Given the one-step prediction $\mathbf{x}_1^{\text{pred}}$ and a factor \mathbf{L} satisfying $\mathbf{B} = \mathbf{L}\mathbf{L}^\top$, we draw Gaussian perturbations $\xi^{(i)} = \mathbf{L}\epsilon^{(i)}$ and evaluate the cost $J(\mathbf{x}_1^{(i)}, \lambda)$ at the perturbed samples $\mathbf{x}_1^{(i)} = \mathbf{x}_1^{\text{pred}} + \xi^{(i)}$. The weights $\omega^{(i)} \propto \exp(-J(\mathbf{x}_1^{(i)}, \lambda))$ form an empirical approximation of the exponentially tilted distribution, and the returned vector

$$\mathbf{g} \approx \mathbb{E}[\xi \mid \text{tilt by } \exp(-J)]$$

is the weighted average of the perturbations. We compute the weights in a numerically stable manner by subtracting ℓ_{\max} before exponentiation.

Algorithm 6 SAMPLETILTEDMEAN

```

1: Input: one-step prediction  $\mathbf{x}_1^{\text{pred}}$ ; factor  $\mathbf{L}$ ; time  $t$ ; guide scale  $\lambda$ ; cost  $J(\cdot, \lambda)$ ; MC size  $S$ ; small  $\varepsilon > 0$ ; schedule  $b_t$ .
2: Output: tilted-mean estimate  $\mathbf{g}$ .
3: Sample  $\{\boldsymbol{\epsilon}^{(i)}\}_{i=1}^S \sim \mathcal{N}(\mathbf{0}, \mathbf{I})$ 
4:  $\sigma(t) \leftarrow \frac{1-t+\varepsilon}{\sqrt{t+\varepsilon}}$ 
5: for  $i = 1$  to  $S$  do
6:    $\boldsymbol{\xi}^{(i)} \leftarrow \mathbf{L}\boldsymbol{\epsilon}^{(i)}$ 
7:    $\mathbf{x}_1^{(i)} \leftarrow \mathbf{x}_1^{\text{pred}} + \boldsymbol{\xi}^{(i)}$ 
8:    $\ell^{(i)} \leftarrow -J(\mathbf{x}_1^{(i)}, \lambda)$ 
9: end for
10:  $\ell_{\max} \leftarrow \max_i \ell^{(i)}$ 
11:  $\omega^{(i)} \leftarrow \exp(\ell^{(i)} - \ell_{\max}), \quad Z \leftarrow \sum_{i=1}^S \omega^{(i)}$ 
12:  $\mathbf{g} \leftarrow b_t \sum_{i=1}^S \frac{\omega^{(i)}}{Z} \boldsymbol{\xi}^{(i)}$ 
13: return  $\mathbf{g}$ 

```

Time complexity. Let d be the latent dimension and let S denote the Monte Carlo sample size. We implement \mathbf{L} via the implicit routine APPLYL (Alg. 5), so each sample requires one application of \mathbf{L} to a vector and one forward evaluation of the cost predictor. If \mathbf{L} is stored in compact form with rank r (in our memory-queue setting, typically $r \leq 2m$), then APPLYL costs $\mathcal{O}(dr + r^2)$, and the total per-step complexity is

$$\mathcal{O}(S(dr + r^2)) + \mathcal{O}(SC_J^{\text{fwd}}),$$

where C_J^{fwd} denotes the cost of a single forward pass of the cost predictor. The remaining operations (computing ℓ_{\max} , forming the normalized weights, and the weighted sum) contribute $\mathcal{O}(S)$ scalar work and $\mathcal{O}(Sd)$ vector accumulations, which are dominated by the two terms above. The memory footprint is $\mathcal{O}(Sd)$ if all samples (and their intermediate vectors) are stored; in practice, this can be reduced to $\mathcal{O}(d)$ by streaming the computation (accumulating ℓ_{\max} and the weighted sum on the fly), at the cost of an additional pass over the S samples.

E. Experiment Setting

E.1. 2D Experimental Setting

We study a synthetic 2D problem on the bounded square domain $\mathcal{X} = [-3.5, 3.5] \times [-3.5, 3.5]$. All densities and costs are represented on a uniform Cartesian grid; we use a 256×256 grid to construct and store the underlying fields, while KL metrics for model selection are evaluated on a separate $N_{\text{grid}} \times N_{\text{grid}}$ grid (default $N_{\text{grid}} = 250$) for a controllable accuracy-speed trade-off.

Data distribution. The data distribution $p_0(\mathbf{x})$ is defined by a smooth Gaussian random field (GRF) on the 256×256 grid. Concretely, we build a grid potential and convert it into a truncated density over \mathcal{X} by exponentiation and numerical normalization: mass outside \mathcal{X} is set to zero and the normalization constant is computed by summing the resulting discrete probabilities on the grid.

Sampling. Sampling is consistent with the truncated-and-renormalized p_0 . We first evaluate the unnormalized log-density on grid nodes, convert it into a discrete probability mass function (PMF), and draw grid indices via multinomial sampling. To reduce lattice artifacts, we add a small uniform jitter within each selected grid cell and clamp samples back to \mathcal{X} .

Cost landscape. The cost function $C(\mathbf{x})$ is generated independently as a smooth GRF on the same 256×256 grid. The field is standardized (zero mean and fixed standard deviation) and queried continuously via bilinear interpolation with border padding. Optionally, we use a peak-shift variant $C(\mathbf{x})$.

Tilted target distribution and KL evaluation. Given p and C , we define the tilted target distribution $q(\mathbf{x}) \propto p_0(\mathbf{x}) \exp(-\alpha C(\mathbf{x}))$ (α denoted as `scale`). For evaluation, we discretize both p_0 and C on an $N_{\text{grid}} \times N_{\text{grid}}$ grid over \mathcal{X} , form a grid PMF for q , and compute divergences between the ground-truth q and the model-induced q obtained by replacing C with the predicted cost \hat{C} : $\text{KL}(q\|\hat{q})$, $\text{KL}(\hat{q}\|q)$, and their symmetric version $\text{SKL} = \frac{1}{2}(\text{KL}(q\|\hat{q}) + \text{KL}(\hat{q}\|q))$. We track these quantities every training step and select checkpoints by the minimum SKL.

Reproducibility. All random seeds are fixed, and the generated GRF fields (for both p and C) can be serialized and reused, ensuring identical experimental settings across runs.

E.2. Vehicle aerodynamic optimization and generation setting

Dataset. We adopt DrivAerNet++ (Elrefaei et al., 2024), a large-scale vehicle aerodynamics dataset based on the parametric DrivAer model. DrivAerNet++ provides thousands of watertight vehicle surfaces together with CFD-derived aerodynamic quantities obtained with OpenFOAM simulations. For each shape, the dataset includes integrated force coefficients such as the drag and lift coefficients (C_d, C_l).

Item	DrivAerNet++ setting used in our experiments
Base geometry	DrivAer parametric vehicle model
Scale	~8,000 vehicle shapes with CFD annotations
CFD solver	OpenFOAM
Outputs used in this paper	Integrated drag coefficient C_d
Target in this paper	Minimize C_d (lower is better)
Usage in this paper	Train cost predictor J_θ

Table 2. Summary of DrivAerNet++ and the aerodynamic quantities used in our vehicle experiments.

Target. Our optimization target is the drag coefficient C_d reported by CFD. We use the standard definition

$$C_d \triangleq \frac{D}{q_\infty A_f}, \quad q_\infty \triangleq \frac{1}{2} \rho_\infty U_\infty^2, \quad (104)$$

where D is the streamwise aerodynamic drag force acting on the vehicle, A_f is the frontal reference area, U_∞ is the freestream speed, and ρ_∞ is the freestream air density. Accordingly, we instantiate the cost as $J(\mathbf{x}) = C_d(\mathbf{x})$.

E.3. Aircraft aerodynamic optimization and generation setting

Dataset. Following Sung et al. (2025), we adopt BLENDEDNET, a high-fidelity aerodynamic dataset for blended-wing-body (BWB) aircraft. It contains 999 unique BWB geometries, each simulated under multiple flight conditions, resulting in 8,830 successfully converged CFD cases. For each geometry–condition pair, the dataset provides integrated force coefficients, including the drag and lift coefficients (C_d, C_l), computed using FUN3D with steady RANS.

Item	BlendedNet setting used in our experiments
Base geometry	Parametric blended-wing-body (BWB) aircraft family
Scale	999 geometries; 8,830 converged CFD cases (multiple conditions per geometry)
Conditioning variables	Flight-condition parameters (e.g., Mach, AoA, altitude / Reynolds length)
CFD solver	FUN3D (steady RANS)
Outputs used in this paper	Integrated C_d, C_l
Target in this paper	Minimize C_d/C_l (lower is better)
Usage in this paper	Train cost predictor J_θ

Table 3. Summary of BlendedNet and the aerodynamic quantities used in our aircraft experiments.

Target. For each geometry under a specified flight condition, we use the standard aerodynamic definitions

$$C_d \triangleq \frac{D}{q_\infty S_{\text{ref}}}, \quad C_l \triangleq \frac{L}{q_\infty S_{\text{ref}}}, \quad q_\infty \triangleq \frac{1}{2} \rho_\infty U_\infty^2, \quad (105)$$

where D and L denote the drag and lift forces, S_{ref} is the reference area, and ρ_∞ and U_∞ are the freestream density and speed, respectively. We evaluate aerodynamic performance using the drag-to-lift ratio C_d/C_l (equivalently maximizing L/D), and instantiate the cost as

$$J(\mathbf{x}) = \frac{C_d(\mathbf{x})}{C_l(\mathbf{x})}, \quad (106)$$

computed under the corresponding flight condition of each sample.

F. Evaluation

F.1. DrivAer Car OpenFOAM Setting

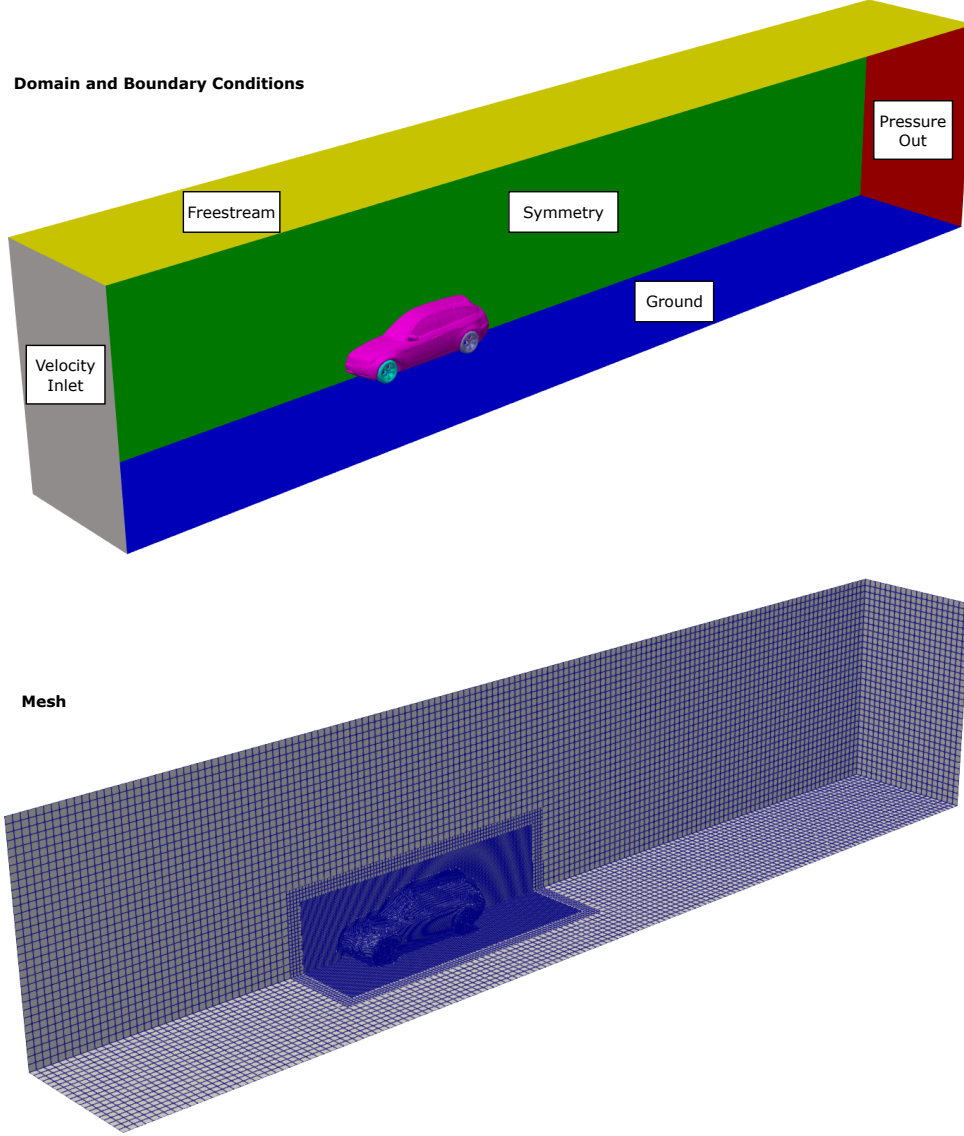


Figure 7. CFD setup. **Top:** computational domain and boundary conditions. **Bottom:** hex-dominant mesh with local refinement around the vehicle and near-wake. Boundary labels correspond to OpenFOAM patches: *Velocity Inlet* (ffminx), *Pressure Out* (ffmaxx), *Symmetry* (ffminy), *Freestream / far-field slip* (ffmaxy, ffmaxz), and *Moving Ground* (ffminz).

Domain and Boundary Conditions. We solve a steady incompressible RANS problem using `simpleFoam`. The inflow speed is set to $U_\infty = 30$ m/s. At the inlet (ffminx), we impose a uniform velocity $\mathbf{U} = (U_\infty, 0, 0)$. At the outlet (ffmaxx), we use an `inletOutlet` condition for \mathbf{U} to robustly handle possible backflow. A symmetry plane is applied on ffminy, while the remaining far-field boundaries (ffmaxy, ffmaxz) use slip conditions to approximate a freestream. To mimic a moving-belt setup, the ground patch (ffminz) is prescribed with $\mathbf{U} = (U_\infty, 0, 0)$. The vehicle body (body2) uses a no-slip wall with $\mathbf{U} = \mathbf{0}$. The wheels (ruotaant, ruotapost) are modeled via `rotatingWallVelocity` with angular speed $\omega = -94$ rad/s about the lateral axis, using the wheel centers specified in the case files. Aerodynamic coefficients are computed using `forceCoeffs` on the body, each wheel, and their union.

Table 4. Boundary conditions for the velocity field \mathbf{U} .

Patch	Physical meaning	\mathbf{U} boundary condition
ffminx	Velocity inlet	fixedValue ($U_\infty, 0, 0$)
ffmaxx	Pressure outlet	inletOutlet (inletValue ($U_\infty, 0, 0$))
ffminy	Symmetry plane	symmetry
ffmaxy	Far-field	slip
ffminz	Moving ground	fixedValue ($U_\infty, 0, 0$)
ffmaxz	Far-field	slip
body2	Car body	fixedValue (0, 0, 0)
ruotaant/ruotapost	Wheels	rotatingWallVelocity ($\omega = -94$ rad/s)

Meshing. As shown in Fig. 7, we employ a hex-dominant background mesh and apply a locally refined region enclosing the vehicle and its near-wake to better resolve separation and vortical structures. Cell sizes transition smoothly from the refined block to the far-field boundaries to control computational cost while maintaining stability. For diagnostics and post-processing, we additionally output standard quantities including y^+ , Q -criterion, and wall shear stress.

Result

F.2. Blender OpenFOAM Setting

Domain and Boundary Conditions. We run steady incompressible RANS simulations using `simpleFoam`. The freestream speed is set to $|\mathbf{U}_\infty| = 50$ m/s. To model an inclined inflow, we prescribe a uniform inlet velocity $\mathbf{U}_\infty = (49.2404, 0, 8.6824)$ m/s, corresponding to a 10° incidence in the x - z plane. At the inlet (ffminx), \mathbf{U} is enforced by a fixed-value condition. At the outlet (ffmaxx), we use `inletOutlet` for \mathbf{U} to improve robustness under possible backflow. A symmetry plane is imposed on ffminy, and the remaining far-field boundaries (ffmaxy, ffminz, ffmaxz) use slip conditions to approximate a freestream. The car surface (body2) is treated as a no-slip wall with $\mathbf{U} = \mathbf{0}$. We compute aerodynamic coefficients using `forceCoeffs` on body2, with drag along (1, 0, 0) and lift along (0, 0, 1).

 Table 5. Boundary conditions for the velocity field \mathbf{U} in the Blender car setup.

Patch	Physical meaning	\mathbf{U} boundary condition
ffminx	Velocity inlet	fixedValue (49.2404, 0, 8.6824)
ffmaxx	Pressure outlet	inletOutlet (inletValue (49.2404, 0, 8.6824))
ffminy	Symmetry plane	symmetry
ffmaxy	Freestream boundary	slip
ffminz	Freestream boundary	slip
ffmaxz	Freestream boundary	slip
body2	blender body	fixedValue (0, 0, 0)

Meshing. As shown in Fig. 8, we employ a hex-dominant background mesh and add a locally refined region that encloses the vehicle and its near-wake. The mesh resolution is increased around the body to better capture separation and wake development, while coarser cells are used in the far field to control cost. For analysis and visualization, we enable additional function objects, including y^+ , Q -criterion, and wall shear stress, and compute time-averaged statistics after an initial transient.

F.3. 3D-printed car and miniature wind tunnel testing

We complement CFD-based evaluation with physical tests in a miniature wind tunnel using 3D-printed vehicles. For each design (before/after optimization, and generations with/without guidance), we fabricate a rigid scaled model and place it at a fixed location in the test section. As illustrated in Fig. 9b, the incoming flow is produced by a fan, seeded by a smoke generator, and then passes through a grille to reduce large-scale non-uniformity before interacting with the vehicle. We record smoke-visualization images from a fixed viewpoint under consistent lighting. To suppress instantaneous fluctuations

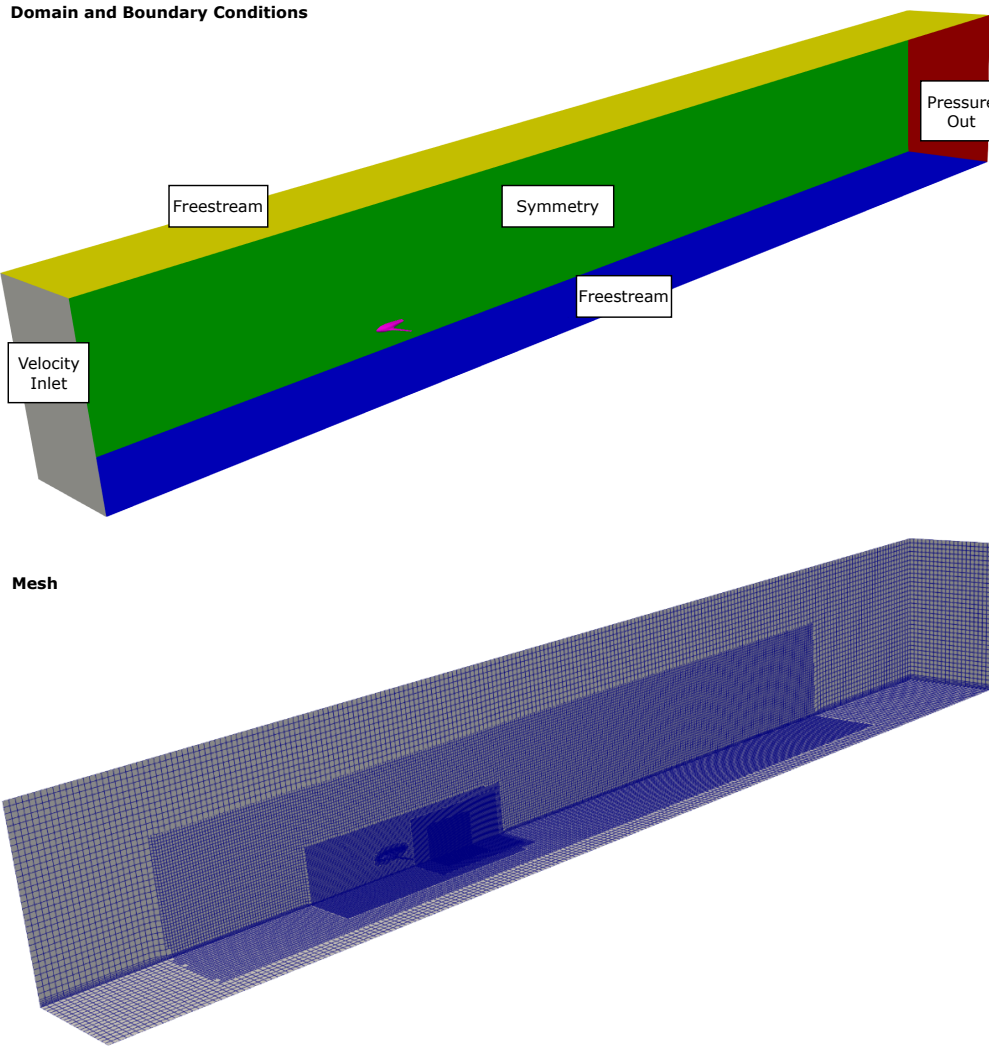


Figure 8. CFD setup for the Blender car. **Top:** computational domain and boundary conditions: *Velocity Inlet* ($ffminx$), *Pressure Out* ($ffmaxx$), *Symmetry* ($ffminy$), and *Freestream* slip walls ($ffmaxy$, $ffminz$, $ffmaxz$). **Bottom:** hex-dominant mesh with local refinement around the vehicle and near-wake.

and measurement noise, we acquire 90 frames per design and compute a time-averaged image, which serves as our primary qualitative indicator of the mean wake structure.

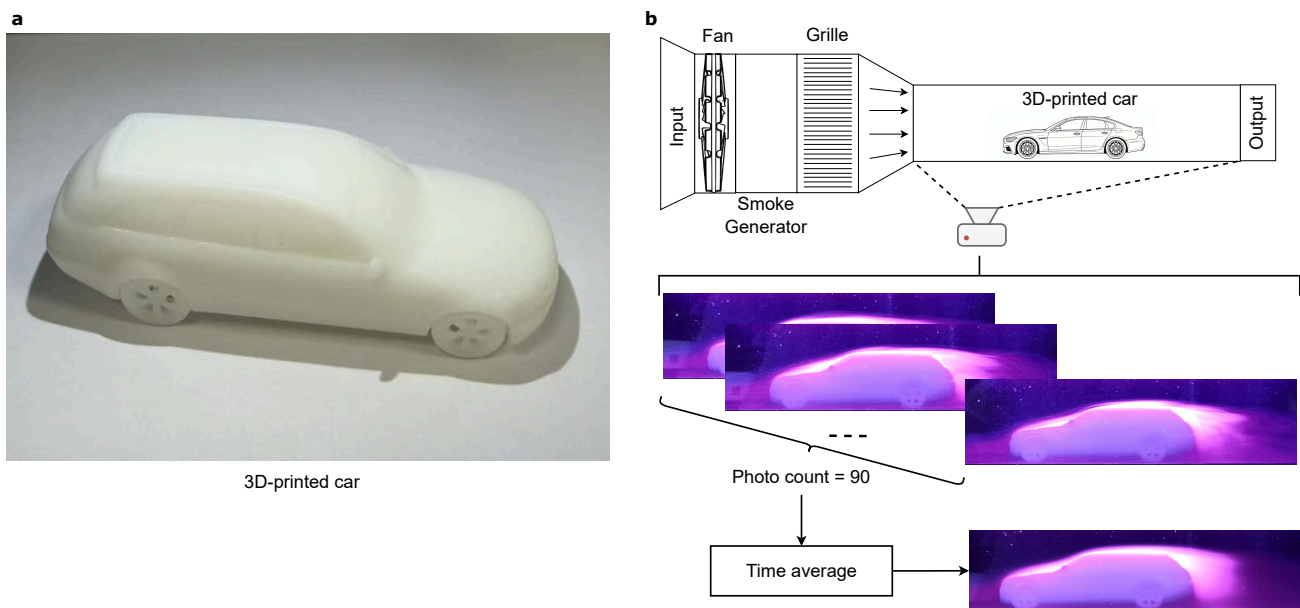


Figure 9. Physical evaluation with a miniature wind tunnel. (a) An example 3D-printed car used for testing. (b) Experimental pipeline: the fan-driven flow is seeded by a smoke generator and conditioned by a grille/flow straightener before entering the test section containing the 3D-printed car. For each design, we capture a sequence of smoke-visualization images from a fixed camera view (*photo count* = 90) and report both representative snapshots and their time-averaged image for comparison.

G. Additional Analysis of Experiment Results

G.1. Why do guided methods with an MSE-trained predictor exhibit a consistent drift?

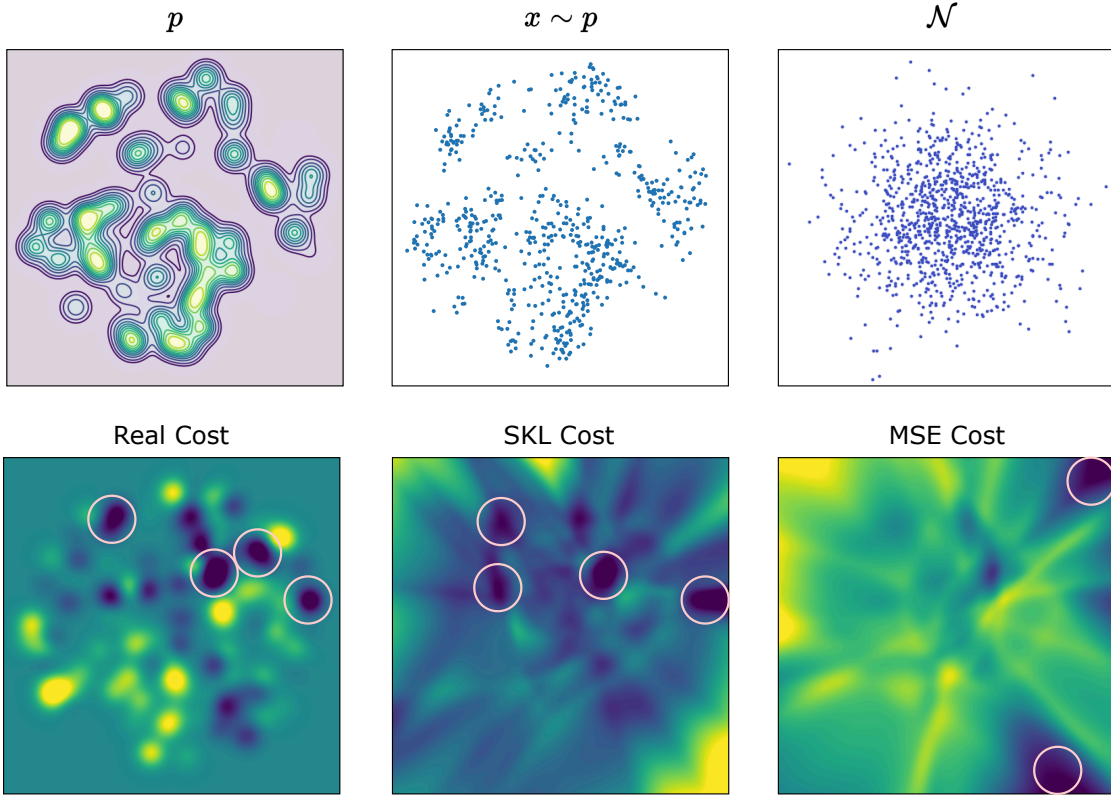


Figure 10. Out-of-support generalization explains the drift of MSE-based guidance. **Top:** the data density p (contours), samples $x \sim p$, and the base noise distribution \mathcal{N} used to initialize generation. **Bottom:** cost landscapes over the *entire* domain: ground-truth (*Real Cost*), SKL-trained predictor (*SKL Cost*), and MSE-trained predictor (*MSE Cost*). All cost maps are normalized for visualization, and circles mark the lowest few minima (global low-cost basins) in each map.

When training the cost predictor, supervision is only available on samples drawn from the data distribution p (top row), i.e., the predictor is learned on the support of p . Consequently, the learned predictor is under-constrained outside the data support and may extrapolate arbitrarily in low-density regions. This distinction becomes crucial for guided generation: sampling is initialized from noise \mathcal{N} and thus inevitably traverses regions far outside the support of p . Therefore, effective guidance requires the predictor to match the *global* low-cost basins of the true cost landscape over the full domain.

The second row visualizes this effect by plotting the cost fields over the entire space and highlighting the lowest few minima after normalization. The SKL-trained predictor better preserves the locations of these global minima compared with the ground-truth cost, while the MSE-trained predictor produces mismatched or spurious minima in out-of-support regions. As a result, guidance computed from the MSE predictor tends to pull trajectories consistently toward incorrect low-cost basins, manifesting as a systematic drift during generation.

H. Offline Reinforcement Learning

H.1. Experiment Setting

We follow the offline planning setup in [Feng et al. \(2025\)](#) to benchmark training-free guidance on offline reinforcement learning tasks. Concretely, we use the D4RL locomotion suite (HalfCheetah, Hopper, Walker2d) under standard dataset regimes (Medium, Medium-Expert, and Medium-Replay), where demonstrations are non-expert mixtures or replay buffers and the goal is to recover high-return behavior from offline data. ([Fu et al., 2020](#); [Janner et al., 2022](#)).

Planner formulation. Our evaluation adopts the Diffuser-style generative planning pipeline: a generative model proposes a length- H state-action sequence, and a critic estimates the discounted return-to-go of the proposed plan; guidance then biases sampling toward higher predicted returns, i.e., sampling from an energy-weighted distribution proportional to $p(\tau) \exp(R(\tau))/Z$ ([Levine, 2018](#)).

Generative model and critic. The base planner is a conditional flow-matching model (CFM) or mini-batch OT-CFM with an affine path $\alpha_t = t, \beta_t = 1 - t$, implemented with an 8-layer Transformer backbone of hidden size 256. It is trained for 10^5 steps with batch size 32, learning rate 2×10^{-4} , and cosine-annealing scheduling. The critic shares the same backbone and uses the last token as the value head; it is trained for 10^4 steps with batch size 64 and learning rate 2×10^{-4} . The discount factor is fixed to 0.99. **In experiments, we use the pretrained model checkpoints released by Feng et al. (2025).**

Planning protocol. We plan with horizon $H = 20$ and stride 1, and intentionally disable commonly used tricks to isolate the effect of guidance. For a fair comparison, all guidance methods share the same pretrained base generative model during evaluation. ([Feng et al., 2025](#)).

Metric and hyperparameter tuning. We report D4RL normalized scores, where 100 corresponds to the expert policy return. ([Fu et al., 2020](#)) ([Feng et al., 2025](#)). Hyperparameters are tuned per method following [Feng et al. \(2025\)](#): covariance-gradient guidances sweep multiple λ_t schedules (e.g., constant/decay families) and global scales; g_{MC} sweeps the reward scaling and uses up to 128 Monte Carlo samples with a small numerical stabilizer; g_{sim-MC} sweeps reward scaling and an assumed conditional standard deviation, and additionally tunes a lightweight schedule/scale on the estimated guidance. ([Feng et al., 2025](#)).

Baselines and Hyperparameter Tuning. We adopt the same four baselines as in the main text, including DPS ([Chung et al., 2022](#)), LGD-MC ([Song et al., 2023](#)), SIM-MC ([Feng et al., 2025](#)), and our method SA-MC. Following [Feng et al. \(2025\)](#), we perform a small hyperparameter sweep over: (i) the flow-matching variant (cfm or ot_cfm); (ii) the number of Monte Carlo samples (16, 64, 128); (iii) the guidance scale (0.1, 1); and (iv) the guidance schedule (original or linear decay). Here *original* refers to the default schedule used in each method. For DPS (Eq. 17) and LGD-MC (Eq. 18), the schedule is $b_t \sigma^2 / \alpha_t$, which equals $(1 - t)/t$ in practice. For SIM-MC (Eq. 19) and SA-MC, the schedule is b_t , which equals $1/(1 - t)$ in practice. The *linear decay* schedule is set to $1 - t$.

H.2. Result and analysis

Following the experimental setting above, we sweep the hyperparameters listed in Sec. H.1 and report, for each method, the *best* score achieved on each task under this sweep. Table 6 summarizes the resulting best-performance comparison across all configurations. Overall, SA-MC achieves the best average normalized score among the compared methods.

Beyond the mean score, SA-MC exhibits stronger *practical reliability*. As shown by the detailed breakdown in Tables 7–10, DPS and LGD-MC can be sensitive to the choice of schedule and scale. In particular, under the method-specific original schedules, DPS and LGD-MC may become numerically unstable for some settings and fail to return a valid evaluation score; such failed cases are marked by “–” in the tables. Switching to the linear-decay schedule alleviates this issue in several tasks, but does not eliminate it entirely, indicating that these methods remain fragile under certain hyperparameter choices. In contrast, SIM-MC and SA-MC yield valid results more consistently across the same sweep, and SA-MC maintains competitive or leading performance across datasets.

For clarity, Tables 7 and 9 report results using OT-CFM under the original and linear-decay schedules, respectively. Tables 8 and 10 report the analogous results using CFM. In all tables, “w/o g ” denotes unconditional sampling without guidance, and reported values are mean \pm standard deviation over evaluation runs.

Table 6. Offline RL results on D4RL locomotion. We report the best normalized score (mean \pm std.) for each method under our hyperparameter sweep described in Sec. H.1. The last row reports the average over all nine tasks. Bold indicates the best result and underline indicates the second best.

		Overall				
		w/o g	DPS	LGD-MC	SIM-MC	SA-MC
Medium-Expert	HalfCheetah	62.3 \pm 17.9	41.8 \pm 17.0	<u>66.5 \pm 0.22</u>	60.6 \pm 16.5	71.0 \pm 14.6
	Hopper	82.8 \pm 22.3	99.1 \pm 13.3	100.4 \pm 18.5	<u>101.7 \pm 18.1</u>	102.1 \pm 17.9
	Walker2d	84.6 \pm 12.6	107.5 \pm 0.5	<u>103.2 \pm 4.7</u>	96.1 \pm 12.7	97.7 \pm 10.8
Medium	HalfCheetah	42.5 \pm 1.0	42.8 \pm 1.1	42.6 \pm 1.0	<u>42.7 \pm 1.2</u>	42.4 \pm 0.9
	Hopper	76.2 \pm 10.7	90.5 \pm 14.0	74.6 \pm 11.2	<u>77.2 \pm 15.9</u>	<u>80.7 \pm 11.4</u>
	Walker2d	68.8 \pm 10.8	79.7 \pm 7.5	76.1 \pm 10.7	77.4 \pm 2.8	78.3 \pm 4.1
Medium-Replay	HalfCheetah	34.9 \pm 3.0	31.6 \pm 14.6	38.3 \pm 1.5	36.0 \pm 2.2	<u>36.2 \pm 1.7</u>
	Hopper	44.1 \pm 6.7	66.4 \pm 6.0	55.1 \pm 11.1	53.6 \pm 15.6	<u>57.6 \pm 8.6</u>
	Walker2d	50.8 \pm 28.3	<u>67.1 \pm 24.3</u>	70.4 \pm 5.4	56.0 \pm 18.7	62.1 \pm 20.0
Average		60.8	69.6	<u>69.7</u>	66.8	69.8

Table 7. OT-CFM with original schedule. D4RL normalized scores (mean \pm std.) for each dataset and environment. “w/o g ” denotes no guidance. “–” indicates runs that produced invalid scores under the corresponding setting.

		OT-CFM, Original Schedule				
		w/o g	DPS	LGD-MC	SIM-MC	SA-MC
Medium-Expert	HalfCheetah	62.3 \pm 17.9	-	-	60.6 \pm 16.5	71.0 \pm 14.6
	Hopper	82.8 \pm 22.3	-	79.5 \pm 19.4	101.0 \pm 17.9	100.7 \pm 18.7
	Walker2d	84.6 \pm 12.6	-	-	86.0 \pm 20.7	87.0 \pm 16.1
Medium	HalfCheetah	41.3 \pm 0.5	41.6 \pm 0.1	41.8 \pm 0.6	41.4 \pm 0.9	41.9 \pm 0.3
	Hopper	54.4 \pm 8.9	-	55.3 \pm 4.5	53.0 \pm 6.5	58.1 \pm 6.0
	Walker2d	68.8 \pm 10.8	-	-	66.6 \pm 15.7	77.0 \pm 9.0
Medium-Replay	HalfCheetah	22.4 \pm 5.0	-	23.5 \pm 6.4	24.4 \pm 6.2	24.5 \pm 8.0
	Hopper	44.1 \pm 6.7	-	-	47.7 \pm 3.4	55.3 \pm 14.3
	Walker2d	31.0 \pm 2.0	-	-	39.3 \pm 20.6	40.3 \pm 20.1

Table 8. CFM with original schedule. D4RL normalized scores (mean \pm std.) for each dataset and environment. “w/o g ” denotes no guidance. “–” indicates runs that produced invalid scores under the corresponding setting.

		CFM, Original Schedule				
		w/o g	DPS	LGD-MC	SIM-MC	SA-MC
Medium-Expert	HalfCheetah	44.9 \pm 3.6	-	-	57.5 \pm 20.2	51.6 \pm 18.9
	Hopper	61.1 \pm 13.1	-	91.7 \pm 17.4	91.1 \pm 23.4	91.9 \pm 24.7
	Walker2d	67.5 \pm 29.5	-	-	90.2 \pm 23.9	94.1 \pm 15.5
Medium	HalfCheetah	42.5 \pm 1.0	42.6 \pm 0.4	41.8 \pm 0.7	41.9 \pm 0.7	42.4 \pm 0.9
	Hopper	76.2 \pm 10.7	-	71.6 \pm 10.6	72.4 \pm 3.9	80.7 \pm 11.4
	Walker2d	68.7 \pm 23.3	-	68.6 \pm 14.5	71.9 \pm 6.8	78.3 \pm 4.1
Medium-Replay	HalfCheetah	34.9 \pm 3.0	-	33.1 \pm 5.5	30.2 \pm 13.6	34.9 \pm 4.4
	Hopper	39.4 \pm 2.6	-	48.0 \pm 13.9	53.6 \pm 15.6	52.6 \pm 13.7
	Walker2d	50.8 \pm 28.3	-	35.6 \pm 8.8	56.0 \pm 18.7	57.8 \pm 19.9

In addition to accuracy and robustness, SA-MC is also more efficient in wall-clock time. Figure 11 compares the time required to generate a 1,000-step trajectory on D4RL locomotion tasks. Compared with the substantial overhead of DPS and LGD-MC relative to unconditional sampling, SA-MC incurs only a modest additional cost (similar to SIM-MC). This efficiency becomes particularly important when scaling to large hyperparameter sweeps and extensive evaluations.

Table 9. OT-CFM with linear-decay schedule. D4RL normalized scores (mean \pm std.) for each dataset and environment. “w/o g ” denotes no guidance.

		OT-CFM, Linear Decay Schedule				
		w/o g	DPS	LGD-MC	SIM-MC	SA-MC
Medium-Expert	HalfCheetah	62.3 \pm 17.9	-	64.5 \pm 10.6	58.3 \pm 18.5	61.8 \pm 16.0
	Hopper	82.8 \pm 22.3	85.8 \pm 16.2	100.4 \pm 18.5	101.7 \pm 18.1	102.1 \pm 17.9
	Walker2d	84.6 \pm 12.6	107.5 \pm 0.5	93.1 \pm 10.8	85.7 \pm 20.2	86.1 \pm 14.0
Medium	HalfCheetah	41.3 \pm 0.5	42.1 \pm 0.7	41.8 \pm 0.6	41.5 \pm 0.7	41.8 \pm 1.2
	Hopper	54.4 \pm 8.9	66.5 \pm 1.7	68.3 \pm 6.3	57.9 \pm 11.6	57.3 \pm 6.2
	Walker2d	68.8 \pm 10.8	75.4 \pm 9.5	76.1 \pm 10.7	69.2 \pm 12.6	67.9 \pm 10.3
Medium-Replay	HalfCheetah	22.4 \pm 5.0	24.6 \pm 9.2	28.1 \pm 4.4	22.1 \pm 3.2	25.5 \pm 5.2
	Hopper	44.1 \pm 6.7	66.4 \pm 6.0	49.8 \pm 10.3	52.3 \pm 6.2	57.6 \pm 8.6
	Walker2d	31.0 \pm 2.0	67.1 \pm 24.3	43.5 \pm 16.6	40.1 \pm 19.2	45.1 \pm 15.5

Table 10. CFM with linear-decay schedule. D4RL normalized scores (mean \pm std.) for each dataset and environment. “w/o g ” denotes no guidance.

		CFM, Linear Decay Schedule				
		w/o g	DPS	LGD-MC	SIM-MC	SA-MC
Medium-Expert	HalfCheetah	44.9 \pm 3.6	41.8 \pm 17.0	66.5 \pm 0.22	51.9 \pm 19.7	62.4 \pm 24.0
	Hopper	61.1 \pm 13.1	99.1 \pm 13.3	98.8 \pm 18.6	94.4 \pm 21.7	91.8 \pm 19.0
	Walker2d	67.5 \pm 29.5	103.2 \pm 7.6	103.2 \pm 4.7	96.1 \pm 12.7	97.7 \pm 10.8
Medium	HalfCheetah	42.7 \pm 1.5	42.8 \pm 1.1	42.6 \pm 1.0	42.7 \pm 1.2	42.2 \pm 0.7
	Hopper	76.2 \pm 10.7	90.5 \pm 14.0	74.6 \pm 11.2	77.2 \pm 15.9	74.9 \pm 4.0
	Walker2d	68.7 \pm 23.3	79.7 \pm 7.5	72.5 \pm 12.6	77.4 \pm 2.8	77.5 \pm 4.4
Medium-Replay	HalfCheetah	34.9 \pm 3.0	31.6 \pm 14.6	38.3 \pm 1.5	36.0 \pm 2.2	36.2 \pm 1.7
	Hopper	39.4 \pm 2.6	49.5 \pm 11.8	55.1 \pm 11.1	52.2 \pm 7.6	55.7 \pm 19.5
	Walker2d	50.8 \pm 28.3	66.2 \pm 27.8	70.4 \pm 5.4	50.9 \pm 21.4	62.1 \pm 20.0

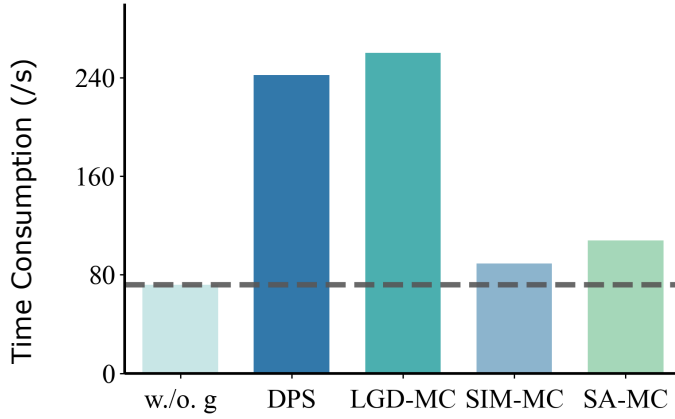


Figure 11. Runtime overhead of guidance on D4RL locomotion. Wall-clock time (seconds) to generate a 1,000-step trajectory. The dashed line denotes the unconditional baseline (w/o g). Lower is better.